Kennicutt-Schmidt relation of galaxies over 13 billion years in the COLIBRE hydrodynamical simulations

Claudia del P. Lagos[1,2★], Joop Schaye,[3] Matthieu Schaller,[3] Danail Obreschkow,[1] Yannick M. Bahé,[4] Alejandro Benítez-Llambay,[5] Evgenii Chaikin,[3] Camila Correa,[3] Timothy A. Davis,[6] Carlos S. Frenk,[7] Filip Huško,[3] Melanie Kaasinen,[8] Robert J. McGibbon,[3] Kyle Oman,[7] Sylvia Ploeckinger,[9] Alexander J. Richings,[10,11] James W. Trayford,[12] Jing Wang,[13] Ruby J. Wright[1]

[1]*International Centre for Radio Astronomy Research (ICRAR), M468, University of Western Australia, 35 Stirling Hwy, Crawley, WA 6009, Australia.*
[2]*Cosmic Dawn Center (DAWN), Denmark.*
[3]*Leiden Observatory, Leiden University, PO Box 9513, 2300 RA Leiden, the Netherlands.*
[4]*School of Physics and Astronomy, University of Nottingham, University Park, Nottingham NG7 2RD, UK.*
[5]*Dipartimento di Fisica G. Occhialini, Università degli Studi di Milano Bicocca, Piazza della Scienza, 3 I-20126 Milano MI, Italy.*
[6]*Cardiff Hub for Astrophysics Research & Technology, School of Physics & Astronomy, Cardiff University, Queens Buildings, Cardiff CF24 3AA, UK.*
[7]*Department of Physics, Institute for Computational Cosmology, Science Laboratories, Durham University, South Road, Durham, DH1 3LE, UK.*
[8]*Research School of Astronomy and Astrophysics, Australian National University, Canberra, ACT 2611, Australia.*
[9]*Department of Astrophysics, University of Vienna, Turkenschanzstrasse 17, 1180 Vienna, Austria.*
[10]*Centre for Data Science, Artificial Intelligence and Modelling, University of Hull, Cottingham Road, Hull, HU6 7RX, UK.*
[11]*E. A. Milne Centre for Astrophysics, University of Hull, Cottingham Road, Hull, HU6 7RX, UK.*
[12]*Institute of Cosmology and Gravitation, University of Portsmouth, Dennis Sciama Building, Burnaby Road, Portsmouth PO1 3FX, UK.*
[13]*Kavli Institute for Astronomy and Astrophysics, Peking University, Beijing 100871, China.*

arXiv:2512.11309v2 [astro-ph.GA] 19 May 2026

Accepted XXX. Received YYY; in original form ZZZ

ABSTRACT

We investigate the correlation between star formation rate (SFR) surface density and gas surface density (known as the Kennicutt–Schmidt, KS, relation) at kiloparsec (kpc) scales across cosmic time ($0 \leq z \leq 8$) for galaxies with stellar masses $> 10^9\,\mathrm{M}_\odot$, using the COLIBRE state-of-the-art cosmological hydrodynamical simulations. These simulations feature on-the-fly non-equilibrium chemistry coupled to dust grain evolution and detailed radiative cooling down to ≈ 10 K, enabling direct predictions for the atomic (H I) and molecular (H_2) KS relations. At $z \approx 0$, COLIBRE reproduces the observed (spatially-resolved) KS relations for H I and H_2, including the associated scatter, which we predict to be significantly correlated with stellar surface density, local specific SFR (sSFR), and gas metallicity. We show that the H I KS relation steepens for lower-mass galaxies, while the H_2 KS relation shifts to higher normalisation in galaxies with higher sSFRs. The H_2 depletion time decreases by a factor of ≈ 20 from $z = 0$ to $z = 8$, primarily due to the decreasing gas-phase metallicity. This results in less H_2 and more H I being associated with a given SFR at higher redshift. We also find that galaxies with higher sSFRs have a larger molecular gas content and higher star formation efficiency per unit gas mass on kpc scales. The predicted evolution of the H_2 depletion time and its correlation with a galaxy's sSFR agree remarkably well with observations in a wide redshift range, $0 \leq z \leq 5$.

Key words: galaxies: ISM – galaxies: star formation – galaxies: evolution – galaxy: formation

1 INTRODUCTION

The connection between star formation and the interstellar medium (ISM) of galaxies is one of the most fundamental questions in extragalactic astronomy. Many surveys have been dedicated to understanding how the star formation rate (SFR) of galaxies, either in a global or in a spatially resolved manner, is connected to the different phases of the ISM (see Tacconi et al. 2020 and Schinnerer & Leroy 2024 for recent reviews).

In the local Universe the SFR correlates strongly with the molecular hydrogen (H_2) content, with the intrinsic scatter being significantly smaller than for the correlations obtained with either atomic hydrogen (H I) or total neutral hydrogen (H I+H_2) (e.g. Leroy et al. 2008; Bigiel et al. 2008; Schruba et al. 2011; Pessa et al. 2021). These relations have been studied at scales from a few hundred parsecs (pc) to a kilo pc (kpc) through correlating the surface densities of SFR, $\Sigma_{\rm SFR}$, and gas, $\Sigma_{\rm gas}$, in many tens of galaxies in the local Universe. This relation is known as the Kennicutt-Schmidt (KS) relation, named after the seminal works of Schmidt (1959) and Kennicutt (1983, 1989). Establishing how the KS relation evolves to higher redshift, z, for either H I or H_2, has been challenging, with the samples in which a resolved KS relation can be measured being limited to $\lesssim 10$ galaxies (e.g. Freundlich et al. 2013; Sharon et al. 2013; Hodge et al. 2015; Sharon et al. 2019; Nagy et al. 2023; Béthermin et al. 2023; Zanella et al. 2024; Gómez et al. 2025). However, from global unresolved measurements of SFR and H_2 mass in thousands of galaxies,

★ E-mail: claudia.lagos@icrar.org

© 2026 The Authors

it has been possible to establish that the two quantities continue to correlate well up to at least $z \approx 5$ (e.g. Tacconi et al. 2020).

Local Universe observations have also helped establish that the KS relation, either in its atomic, molecular or total neutral gas form, displays a scatter that correlates with other galaxy properties; for instance, with the stellar surface density (e.g. Shi et al. 2011, 2018; Dey et al. 2019; Ellison et al. 2020; Lin et al. 2022; Wang et al. 2024; Wong et al. 2024), suggesting that the stellar contribution to the local dynamical state plays a role in the gas-to-star conversion (e.g. Blitz & Rosolowsky 2006; Ostriker et al. 2010). Even when very dense gas traced by HCN (hydrogen cyanide) is used to measure the KS relation, observations continue to show scatter that correlates with other local properties (Usero et al. 2015; Bigiel et al. 2016), confirming that the underlying process of star formation is sensitive to local physical conditions, such as the stellar surface density (e.g. Gallagher et al. 2018; Jiménez-Donaire et al. 2019).

The physical drivers of the atomic and molecular KS relations are not understood. For instance, it is not clear to what extent molecular gas is a prerequisite for star formation as opposed to being a by-product of the cold and dense gas phase normally associated with star formation (Schaye 2004; Glover & Clark 2012). Several state-of-the-art cosmological galaxy formation models and simulations assume that H_2 is required to form stars (e.g. Lagos et al. 2011; Somerville et al. 2015; Lacey et al. 2016; Lagos et al. 2018; Xie et al. 2017; Davé et al. 2019; Feldmann et al. 2023; Lagos et al. 2024); while others only consider dense gas, whether it is molecular or not, and typically assume a fixed threshold density (and/or temperature) for star formation (e.g. Tremmel et al. 2017; Pillepich et al. 2018; Semenov et al. 2018; Agertz et al. 2021). Going beyond a fixed density threshold for star formation, Schaye et al. (2015) attempted to encapsulate the transition from warm to cold ISM into a metallicity-dependent threshold density.

On smaller scales than usually probed by the KS relation results, observations of thousands of individual molecular clouds show very inefficient star formation, with only $\simeq 1\%$ of the gas being converted into stars per dynamical time (see Schinnerer & Leroy 2024 for a review). This inefficiency is challenging to explain (Federrath 2015), with a combination of high turbulence (e.g. Krumholz & McKee 2005; Federrath & Klessen 2012) and efficient early stellar feedback (e.g. Agertz et al. 2013; Segovia Otero et al. 2025) likely needed to cause a quick dispersal of clouds shortly after they have started to form stars.

It is still an open question how to combine the small scale, almost constant efficiency of gas-to-star conversion at the molecular cloud level, with the emergence of the atomic and molecular KS power law on larger scales, at ≈ 1 kpc. Cosmological hydrodynamical simulations have recently attempted to shed light on this problem. Kraljic et al. (2024) used the NewHorizon cosmological hydrodynamical simulation box to study the emergence of the KS relation, focusing primarily on low-mass galaxies, which are more readily captured in their small cosmological volume of $(16\,\mathrm{Mpc})^3$. They found the local gas turbulence to be a key driver of the scatter in the KS relation. This is perhaps unsurprising given the explicit dependence of the star formation efficiency on gas turbulence in their underlying star formation model. They also found that the observed slope of the KS relation at $z = 0$ is only established in their simulation at $z \approx 2 - 3$. More studies like this are needed to understand how general these results may be.

In this paper, we use a new suite of cosmological hydrodynamical simulations, COLIBRE (Schaye et al. 2026; Chaikin et al. 2026) to study the emergence of the atomic, molecular and total neutral gas KS relations, including their scatter. COLIBRE is especially well suited for this study as it includes a sophisticated model of the ISM that takes into account non-equilibrium chemistry of H and He coupled with a live dust model and gas cooling that tracks gas temperatures down to ≈ 10 K and accounts for self-shielding and local sources of radiation (Ploeckinger et al. 2025; Trayford et al. 2025). This means that the H I and H_2 contents of the gas are *predictions* of the simulation. Previous generations of cosmological hydrodynamical simulations did not directly model the formation of H I and H_2 which could only be included in post-processing, imposing chemical and thermal equilibrium (e.g. Lagos et al. 2015; Diemer et al. 2017; Davé et al. 2020). Richings et al. (2022) show that these assumptions fail catastrophically at the high densities and low temperatures typical of the H_2-dominated gas, with differences up to an order of magnitude in the expected abundance of H I and H_2 in that regime. COLIBRE also includes a range of volumes and resolutions that allow us to probe a very large dynamic range in stellar mass, from dwarf galaxies to the most massive galaxies in the universe. COLIBRE uses a star formation model that assumes a fixed efficiency of gas conversion per free fall time of 1%, and hence the emergence of molecular and atomic KS relations is not at all trivial.

This paper is organised as follows. Section 2 presents the COLIBRE simulations used in this work, briefly describing the physical models included. Section 2 also describes how we measure the KS relation and some of the other resolved properties of interest, such as gas metallicity and stellar surface density. Section 3 presents a detailed study of what COLIBRE predicts for the atomic, molecular and total neutral KS relations at $z = 0$, including correlations that arise between other resolved properties and the scatter of the KS relation. Section 3 also presents a comprehensive comparison with observations of the local Universe that probe the zero point and scatter of the KS relation. Section 4 focuses on the predicted redshift evolution of the KS relation from $z = 8$ to $z = 0$, comparing with observations where possible, and exploring the correlation between the scatter of the KS relation and third parameters, such as gas metallicity and stellar surface density. Section 5 presents our conclusions. In Appendix A, we present extensive convergence tests of the KS relation.

2 THE COLIBRE SIMULATIONS

COLIBRE is a suite of cosmological hydrodynamical simulations of varying volume and resolution. A key aspect of COLIBRE is the leap in the sophistication of the modelling of several "subgrid" modules compared to the previous generation of simulations in large cosmological volumes. Subgrid modules encapsulate the physics that happens below the resolution scale of the simulation and include (i) radiative cooling and heating; (ii) the formation, growth and destruction of dust grains; (iii) star formation from unstable gas; (iv) stellar mass loss and the rates of supernova (SN) Ia; (v) stellar winds, radiation pressure from starlight, and HII regions, i.e. stellar feedback processes that start earlier than SN feedback; (vi) SN feedback; (vii) black holes (BHs); (viii) Active Galactic Nuclei (AGN) feedback; (ix) turbulent diffusion. Below we summarise the main characteristics of the subgrid physics modules. We refer to Schaye et al. (2026) for a full description:

- *Numerical setting*. The COLIBRE simulation suite uses the SWIFT code (Schaller et al. 2024) with the Sphenix Smoothed Particle Hydrodynamics (SPH) formulation for hydrodynamics (Borrow et al. 2022) and a fourth-order fast multipole method for gravity (Dehnen 2014). It includes both baryonic and dark matter (DM) particles, with four times more DM than baryonic particles, which

helps suppress spurious transfer of energy from DM to stellar particles and hence improves the effective resolution for the baryonic component (Ludlow et al. 2019, 2021, 2023). Neutrino effects are modelled semi-linearly to account for their influence on structure growth (Ali-Haïmoud & Bird 2013).

• *Radiative cooling* is allowed down to ≈ 10 K. Cooling is computed using an updated version of the CHIMES chemical network (Richings et al. 2014b,a), integrated into the HYBRID-CHIMES framework (Ploeckinger et al. 2025). The model treats non-equilibrium hydrogen and helium chemistry explicitly and uses equilibrium tables for metal cooling, corrected for non-equilibrium free-electron densities. It includes molecular hydrogen formation, photoionisation, photodissociation, photoelectric heating by dust, and shielding by gas and dust, using a local Jeans column approximation (Schaye 2001; Ploeckinger & Schaye 2020). Radiation sources include the Cosmic Microwave Background (CMB), the UV/X-ray background (Faucher-Giguère 2020), and a local interstellar radiation field (Ploeckinger et al. 2025).

• *Dust evolution* is modelled on-the-fly using six dust species (three compositions, two sizes), following Trayford et al. (2025). Dust grains are produced by Asymptotic Giant Branch (AGB) stars (Dell'Agli et al. 2017) and core-collapse supernovae (CCSNe; Zhukovska et al. 2008), and grow via gas accretion following Hirashita & Voshchinnikov (2014). Destruction occurs via sputtering (Tsai & Mathews 1995), stellar feedback, and astration. Grain-grain collisions lead to shattering and coagulation (Aoyama et al. 2017; Granato et al. 2021). The dust physics is coupled to the chemistry and cooling modules.

• *Star formation:* follows a gravitational instability criterion (Nobels et al. 2024), based on the local thermal and turbulent velocity dispersions. Specifically, gas particles are only eligible for star formation if they satisfy

$$\alpha \equiv \frac{\sigma_{\rm th}^2 + \sigma_{\rm turb}^2}{G\,\langle N_{\rm ngb}\rangle^{2/3}\, m_{\rm g}^{2/3}\, \rho_{\rm g}^{2/3}} < 1, \tag{1}$$

where $\sigma_{\rm th}$ and $\sigma_{\rm turb}$ are the particle's 3D thermal and turbulent velocity dispersions, respectively. $N_{\rm ngb}$ is the weighted mean number of neighbours in the SPH kernel, which is about 65 for a quartic spline SPH kernel adopted in COLIBRE. $m_{\rm g}$ is the mean, initial gas particle mass (which we list in Table 1 for the runs used in this work). $\rho_{\rm g}$ is the gas density. $\sigma_{\rm th}$ and $\sigma_{\rm turb}$ are computed from a gas particle's temperature and the local inter-particle velocity (peculiar plus Hubble) dispersion. Gas that meets the criterion in Eq. 1 is stochastically converted into stars using a Schmidt (1959) law ($\rho_{\rm SFR} \propto \rho_{\rm gas}/\tau_{\rm ff}$) with a fixed efficiency of 1% per free-fall time, $\tau_{\rm ff}$. The free-fall time scales as $\rho_{\rm gas}^{-0.5}$, so $\rho_{\rm SFR} \propto \rho_{\rm gas}^{3/2}$.

Because the instability criterion is evaluated at the resolution limit, the instability requirement in Eq. 1 enables higher-resolution runs to probe denser ISM conditions. This also means that as the resolution increases, a larger fraction of the SFR happens in denser gas compared to lower resolution runs (which we show in § 3.1). Nobels et al. (2024), using a suite of idealised galaxy simulations, demonstrated that coarse-grained quantities, such as the observable Kennicutt-Schmidt law on kpc scales, can still converge with the resolution. We demonstrate that this is indeed the case using the fully cosmological simulations COLIBRE (see Appendix A1).

• *Chemical enrichment* models mass loss from Asymptotic Giant Branch (AGB) stars, core collapse SNe, and SNIa using updated nucleosynthetic yields (Correa et al. 2026). Tracked elements include the 11 cooling-dominant species (Wiersma et al. 2009), s-process elements (Ba, Sr), and r-process element (Eu). The SNIa rate follows an exponential delay-time distribution. The model uses metallicity-dependent stellar lifetimes (Portinari et al. 1998), with SNIa yields from the W7 model of Leung & Nomoto (2019), core collapse SNe yields from Nomoto et al. (2006, 2013), and pre-SN winds from Kobayashi et al. (2006). C and Mg yields are scaled by 1.5 for massive stars to match APOGEE observations (Jönsson et al. 2018).

• *Turbulent diffusion* is included to model small-scale mixing of metals and dust, following a diffusion approach motivated by Kolmogorov turbulence (Martínez-Serrano et al. 2008; Greif et al. 2009; Shen et al. 2010). The diffusion coefficient is tied to the local velocity shear, with the strength calibrated to reproduce Milky Way abundance patterns (Correa et al. 2026).

• *Stellar feedback:* includes early feedback from stellar winds, radiation pressure, and HII regions (Benítez-Llambay et al. 2026). Core collapse SN feedback includes a stochastic thermal component (Dalla Vecchia & Schaye 2012, with updates) and a kinetic component to drive turbulence (Chaikin et al. 2023). SNIa feedback uses the same thermal model to prevent numerical overcooling.

• *Black hole growth and AGN feedback:* The fiducial simulations use the black holes and thermal AGN feedback following Booth & Schaye (2009) and Bahé et al. (2022), with modifications to improve the sampling of feedback from low-mass black holes. A subset of runs uses a hybrid AGN feedback model with both thermal and kinetic jets, and black hole spin tracking (Huško et al. 2026).

All feedback parameters are calibrated to reproduce the galaxy stellar mass function, galaxy sizes, and black hole masses at redshift zero, as described in Chaikin et al. (2026).

The adopted cosmology is consistent with the DES Y3 "3×2pt + All Ext." ΛCDM constraints (Abbott et al. 2022). This assumes a flat universe with key parameters: $H_0 = 68.1$ km/s/cMpc, $\Omega_{\rm m} = 0.306$, $\Omega_{\rm b} = 0.0486$, $\Omega_\Lambda = 0.693922$, $\sigma_8 = 0.807$, $n_{\rm s} = 0.967$, $\Sigma\, m_\nu\, c^2 = 0.06$ eV (corresponding to one massive plus two massless neutrinos). The initial baryonic composition assumes $X = 0.756$ and $Y = 0.244$.

Structure identification proceeds in three stages:

• Friends-of-Friends (FoF): Identifies DM haloes using a standard linking length of 0.2 times the mean DM particle separation. Baryonic particles are linked to the nearest DM particle in a halo. Groups with < 32 particles are discarded.

• HBT-HERONS (Forouhar Moreno et al. 2025) Tracks subhaloes across snapshots using a hierarchical bound-tracing approach, improving on HBT+ (Han et al. 2012, 2018). It excels at identifying satellite subhaloes near halo centres and avoids issues like artificial mass fluctuations at pericentres (Forouhar Moreno et al. 2025), which can affect the reconstruction of merger trees (Chandro-Gómez et al. 2025).

• SOAP (McGibbon et al. 2025): Calculates halo and galaxy properties within various 3D and projected apertures. The default aperture for galaxy properties used in this work is a sphere of radius 50 proper kpc (pkpc), centred on the most bound particle. Spherical over-density masses are also computed.

The combination of FoF, HBT-HERONS, and SOAP provides a detailed and robust catalogue of halo and galaxy properties, that enables a consistent post-processing of COLIBRE simulation data. From the SOAP catalogues, we use stellar masses, instantaneous SFRs, H I and H_2 masses. We also use these properties to define the specific SFR, sSFR ≡ SFR/$M_\star$.

In this study, we select all galaxies with $M_\star > 10^9\,{\rm M}_\odot$ and SFR > 0 to construct their resolved KS relation. We apply the same selection to snapshots from $z = 0$ to $z = 8$. This selection yields 106,572 galaxies at $z = 0$ in the L200m6 box, with the number of galaxies

increasing to 120, 398 at $z \approx 0.5$, followed by a steady decrease to 289 at $z = 8$. Appendix A1 presents a convergence study that explains our reasoning for choosing $M_\star > 10^9\,\mathrm{M}_\odot$ as our minimum stellar mass for this analysis.

We make reference throughout this work to gas particles belonging to the hot ionised medium (HIM), warm neutral medium (WNM), and cold neutral medium (CNM). For simplicity, these phases are defined purely by gas temperature, acknowledging that this classification does not uniquely map onto ionisation state (e.g. the WNM may contain ionised gas and the HIM may contain neutral gas; see Fig. 3). Specifically, we define the phases as follows:

$$\begin{aligned} \mathrm{HIM} &: T \geq 10^{4.5}\,\mathrm{K} \\ \mathrm{WNM} &: 10^3\,\mathrm{K} < T < 10^{4.5}\,\mathrm{K}, \\ \mathrm{CNM} &: T \leq 10^3\,\mathrm{K}. \end{aligned} \tag{2}$$

2.1 COLIBRE runs used in this work

Table 1 presents the COLIBRE runs used in this work. Throughout this paper, we will be primarily using the L200m6 run (using a cubic volume of 200 comoving Mpc on a side, and an initial mean particle mass of $10^6\,\mathrm{M}_\odot$). When extending the lower stellar mass limit from $10^9\,\mathrm{M}_\odot$ to $10^8\,\mathrm{M}_\odot$, we also employ the higher resolution run L025m5 (a cubic volume of 25 comoving Mpc on a side, and an initial mean particle mass of $10^5\,\mathrm{M}_\odot$). In Appendix A1, we use the L025 runs of different resolutions to study how well converged the predicted KS relations are with the numerical resolution. Throughout this work, we primarily use the "Thermal AGN feedback" runs of COLIBRE. Schaye et al. (2026) present the full suite of COLIBRE runs, which include more boxes and variations with the "hybrid AGN feedback" model. AGN feedback in COLIBRE primarily affects massive galaxies, and the varying AGN feedback models have the greatest impact on the population of massive, quenching/quenched galaxies. We confirm in Appendix A2 that the Thermal and Hybrid AGN feedback models predict KS relations at $z = 0$ that are almost indistinguishable from each other. Thus, throughout this paper we only analyse runs that adopt the Thermal AGN feedback model.

2.2 Constructing resolved maps

We implement several different ways of computing resolved maps of HI, H_2, SFR, stellar mass, gas metallicity, and gas velocity dispersion, which we describe and compare in Appendix A3. This is done for the purpose of testing the dependence of the KS relation on the way in which radial profiles are computed. We find very good agreement of the KS relation among different methods, and hence we limit ourselves to using the one described below.

Annuli on face-on galaxy: We first orient galaxies to be face-on using their stellar angular momentum vector. The latter is computed using all bound stellar particles within the 50 pkpc spherical aperture, centred on the most bound particle. We then take concentric rings of width Δr, and those are extracted out to 50 pkpc. From the particles belonging to each ring, we measure the HI, H_2, stellar mass, SFR and dust content of the ring, by summing their masses and SFRs. For the total dust mass, we sum the masses in the 6 dust species. For the metallicity, we compute the total number of oxygen atoms and divide by the total number of hydrogen atoms associated with gas particles in the ring that have a temperature $< 10^{4.5}$ K and $> 0.1\,\mathrm{cm}^{-3}$, respectively, excluding metals locked in dust. We then multiply by a factor of 12 to obtain the metallicity in observer units of $12 + \log_{10}(\mathrm{O/H})$. We also save the number of particles that are used for these calculations in each ring and include only annuli with a number of gas particles larger than $N_{\rm min}$.

Our fiducial parameters are $\Delta r = 1$ proper kpc and $N_{\rm min} = 10$ particles. Appendix A3 shows that our results are insensitive to the precise values if they are within $\Delta r = 0.5-2$ kpc and $N_{\rm min} = 1-100$. Note that here we do not place constraints on the vertical distance from the disk plane and simply take all the particles that are bound to the subhalo. To turn masses into surface densities, we simply divide them by the area of the ring. We refer to this method as ANNULI-FACE in Appendix A3 when comparing with other methods.

The resolved maps above are computed for every galaxy in the L200m6 volume with $M_\star > 10^9\,\mathrm{M}_\odot$ and SFR > 0 at different snapshots, but because we place a $N_{\rm min}$ threshold for the minimum number of gas particles per ring, some rings in galaxies do not contribute to the measurement of the KS relation as they are too gas poor.

With these resolved maps, we define the surface densities of SFR ($\Sigma_{\rm SFR}$), stellar mass ($\Sigma_\star$), H I ($\Sigma_{\rm HI}$), H_2 ($\Sigma_{\rm H_2}$), total neutral gas ($\Sigma_{\rm HI+H_2}$), dust ($\Sigma_{\rm dust}$), the local gas metallicity $12 + \log_{10}(\mathrm{O/H})$ and local specific SFR ($s\Sigma_{\rm SFR} = \Sigma_{\rm SFR}/\Sigma_\star$). We also compute the cool gas vertical velocity dispersion profile, by selecting only the gas particles with a temperature $T < 10^{4.5}$ K in each annulus and calculating their mass-weighted velocity dispersion:

$$\sigma_{\rm cool} = \sqrt{\frac{\Sigma\left(v_{\rm z,i}^2 + \sigma_{\rm th}^2\right) m_i}{\Sigma\, m_i}}, \tag{3}$$

where $v_{\rm z,i}$ is the velocity component of gas particle i parallel to the stellar angular momentum vector in the centre-of-mass rest frame of the galaxy, $\sigma_{\rm th} = \sqrt{k_{\rm B}\,T/\mu\, m_{\rm H}}$ is the one-dimensional thermal velocity dispersion, m_i is its mass, T its temperature, $k_{\rm B}$ is Boltzmann's constant, μ is the atomic weight and $m_{\rm H}$ is the hydrogen atom's mass. We tested including limits on the distance of the gas particles to the midplane of the galaxy disk, following the method presented in Jiménez et al. (2023) for the EAGLE simulations, but we do not see a noticeable effect on our results. For simplicity, we thus do not include a limit on distance to the midplane.

Fig. 1 shows examples of $z = 0$ galaxies in the L025m6 simulation with their corresponding H I and H_2 KS relations. Face-on and edge-on images (top and middle panels) were built with R-package SWIFT[1]. Individual symbols in the bottom panels correspond to individual rings in the example galaxies using the ANNULI-FACE method to measure the KS relation. In Fig. B1 we show additional examples of star-forming and passive galaxies, with the latter still having some low-level SFR. In general, we find that in a single galaxy, the H I KS relation has a lower amplitude and a similar or steeper slope than the H_2 KS relation. We will quantify these trends in § 3.

We measure the correlation between $\Sigma_{\rm SFR}$ and other spatially resolved properties with the deviations from the primary KS relations. The idea is to understand how the scatter of the KS relation correlates with other resolved properties and to pinpoint the strongest correlations. This has been done in the past in observations to tease out the dependence of the scatter of one resolved scaling relation on another resolved property (e.g. Ellison et al. 2020). With this in mind, we define:

- ΔSFE: we fit power laws to the relations between $\Sigma_{\rm SFR}$ and $\Sigma_{\rm HI}$, $\Sigma_{\rm H_2}$ or $\Sigma_{\rm HI+H_2}$, using a χ^2-minimisation in log-space. We refer

[1] The code is publicly available at https://github.com/obreschkow/swift.

Table 1. COLIBRE simulations used in this paper. The columns list: (1) the name of the simulation, (2) comoving box size (L), (3) number of initial baryon (N_b) and (4) DM particles (N_{DM}), (5) initial mean particle masses of gas and (6) dark matter, (7) comoving gravitational softening length (ϵ_{com}) and (8) the maximum proper gravitational softening length (ϵ_{prop}). Here, "Thermal" refers to runs using the thermal AGN feedback model, while "Hybrid" refers to runs using the AGN feedback model of Huško et al. (2026). Our fiducial resolution is m6, and unless otherwise stated, L200m6 is the default simulation used for the analysis in this paper. To make this decision visually clear, we highlight the name of that simulation in bold.

(1)	(2)	(3)	(4)	(5)	(6)	(7)	(8)
Name Units	L [cMpc]	N_b	N_{DM}	gas particle mass [$M_\odot$]	DM particle mass [$M_\odot$]	ϵ_{com} [ckpc]	ϵ_{prop} [pkpc]
L025m5 (Thermal)	25	752^3	4×376^3	2.30×10^5	3.03×10^5	0.9	0.35
L025m6 (Thermal)	25	376^3	4×376^3	1.84×10^6	2.42×10^6	1.8	0.7
L025m7 (Thermal)	25	188^3	4×188^3	1.47×10^7	1.94×10^7	3.6	1.4
L050m6 (Thermal)	50	752^3	4×752^3	1.84×10^6	2.42×10^6	1.8	0.7
L050m6 (Hybrid)	50	752^3	4×752^3	1.84×10^6	2.42×10^6	1.8	0.7
L200m6 (Thermal)	200	3008^3	4×3008^3	1.84×10^6	2.42×10^6	1.8	0.7

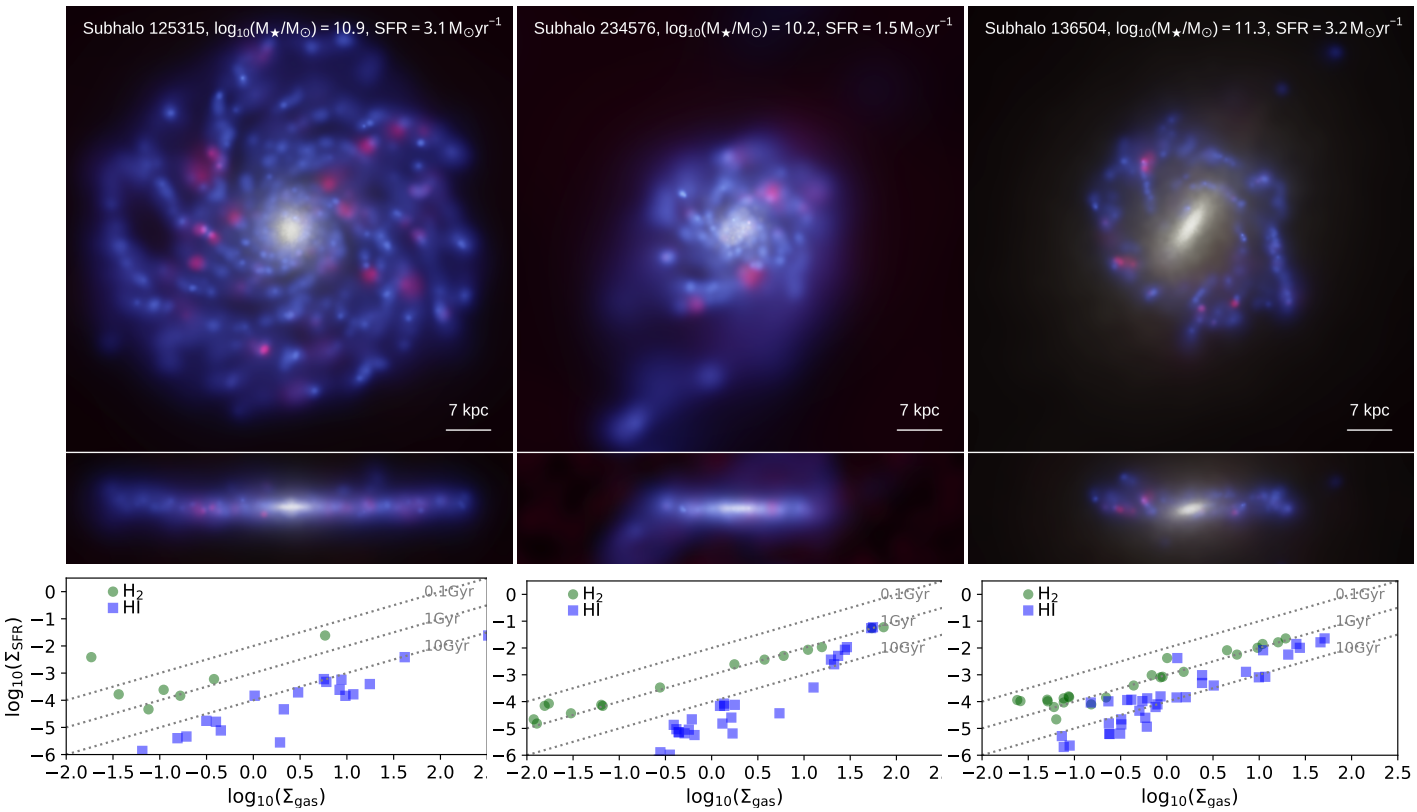

Figure 1. Three example galaxies at $z = 0$ in the L025m6 COLIBRE simulation used in this work. The top and middle panels show face-on and edge-on views of the gas and stellar disk, which were produced using R-package SWIFT. The gas is coloured by the ionisation fraction, with blue indicating neutral gas (H I + H_2), and red ionised gas (primarily HII regions when the red compact regions are in the disk). The stellar component is shown with a gold colour, with the intensity of the colour scaling on the stellar mass density. Each figure shows at the top the stellar mass and SFR of the subhalo and the subhalo index within the SOAP catalogue. We also indicate with a white bar a physical scale for reference. The bottom panels show the individual H I (blue squares) and H_2 (green circles) KS tracks of the galaxies at the top. The tracks are computed using our fiducial ANNULI-FACE method. In the bottom panels, Σ_{SFR} and Σ_{gas} are in units of $M_\odot\,yr^{-1}\,kpc^{-2}$ and $M_\odot\,pc^{-2}$, respectively. The dotted lines indicate fixed depletion times of 0.1, 1 and 10 Gyr as labelled. The left and middle galaxies are examples of normal star-forming galaxies, while the one on the right is an example of a strong bar galaxy that has emptied most of its inner region.

to these fits as KS_{HI}, KS_{H_2} and KS_{HI+H_2}. Using these fits, we then define Δ SFE = $\log_{10}(\Sigma_{SFR}) - KS_x$, with x being HI, H_2 or H I+H_2 (i.e. deviations from the primary relations).

- Δ SFR − prop: characterises the correlations between the deviations from the main relation between $\log_{10}(\Sigma_{SFR})$ and another property. For our purpose, the properties we study are: $\log_{10}(\Sigma_\star)$, $\log_{10}(\Sigma_{dust})$ and $\log_{10}(O/H)$. We also use a linear fit to characterise all these correlations.

Appendix A1 presents a convergence study of the KS relation for HI, H_2 and H I+H_2, using the L025m5, L025m6, L025m7 simulations. For the H_2 KS relation, we see convergence at higher gas surface densities only, $\gtrsim 3\,M_\odot\,pc^{-2}$. Comparing L025m5 and L025m6, we see that the H_2 KS relation converges at $\Sigma_{H_2} \gtrsim 1\,M_\odot\,pc^{-2}$ for the m6 resolution at $z = 0$. The surface density at which the H_2 KS relation at m6 resolution appears to be converged decreases to $0.1\,M_\odot\,pc^{-2}$ at $z = 2$. The median H I KS relation is very well converged at $z = 0$ at all gas surface densities, whereas the scatter tends to increase with increasing resolution. At $z = 2$, however, the H I KS relation at m6 starts to deviate from the results at m5 at $\lesssim 10\,M_\odot\,pc^{-2}$. We will use these surface density thresholds when fitting the KS relation of galaxies in the L200m6 box. We also show that selecting a minimum number of particles per annulus of 10, 50 or 100 has little impact on the resulting KS relation. Unless otherwise stated, throughout this paper, we require a minimum number of gas and stellar particles per annuli of 10.

3 KENNICUTT-SCHMIDT RELATION AT $Z = 0$

In this section, we explore what COLIBRE predicts for the KS relation at $z = 0$ and present a comprehensive comparison with observations. Where necessary, we subtract the contribution of helium from the observational data (typically applied as a constant multiplicative factor) to compare with our predicted surface densities of HI, H_2 and H I+H_2. We also convert from a Salpeter (1955) or Kroupa (2001) IMF to our adopted Chabrier (2003) IMF where necessary. We do this following the conversion factors between different SFR tracers from different IMFs tabulated in Appendix A of Gonzalez-Perez et al. (2014). For stellar masses, we divide the masses derived using an Salpeter (1955) and Kroupa (2001) IMF by 2 and 1.14, respectively, to convert them to a Chabrier (2003) IMF.

3.1 KS relation: comparison with observations and characterisation

We first aim to establish how well COLIBRE matches the local Universe observations of the KS relation. Fig. 2 shows the KS relation at $z = 0$ predicted by COLIBRE, separating the dependence on HI, H_2 and total neutral hydrogen. Here we use the *annuli on face-on galaxy* method. Each galaxy contributes up to 50 data points (i.e. rings) to each plane. However, because we set a minimum number of gas particles per ring to consider it in our analysis, we find that at $z = 0$ the median number of rings contributed to the measurement of the KS relation per galaxy is only 7. Observational data from Walter et al. (2008), Bigiel et al. (2008), Bigiel et al. (2010), Wang et al. (2024), and Ellison et al. (2020) correspond to pixel-wise measurements of sizes 1, 0.75, 0.6, 1 and 0.3 kpc, respectively. Data from Leroy et al. (2013), Sun et al. (2022) and Wong et al. (2024) correspond to annuli of width 1 kpc, which exactly mimics our method. We note, however, that Bigiel et al. (2008) demonstrated that for individual galaxies measurements of the KS relation in pixels vs radial annuli returned indistinguishable results. This agrees with what we show for COLIBRE in Appendix A3.

COLIBRE is in remarkable agreement with observations for all three gas phases. For HI, COLIBRE tends to prefer a lower amplitude, very close to what Wang et al. (2024) reported. The difference between Walter et al. (2008) and Wang et al. (2024) is that the latter includes the more diffuse H I which tends to be missed by interferometric surveys. For H_2, we find that the COLIBRE amplitude is closest to the observational constraints from Ellison et al. (2020) and Wong et al. (2024), which correspond to a depletion time of or slightly above 1 Gyr. We note however, that the differences between different observations are within the typical systematic uncertainties associated with the CO-to-H_2 conversion factor (α_{CO}). For the total neutral hydrogen, we find that COLIBRE's predictions are in between the observational estimates at surface densities $\lesssim 10^{1.5}\,M_\odot\,pc^{-2}$, while at higher densities, there is agreement with Bigiel et al. (2010), which is the only data set available at those surface densities.

The agreement with observations was not guaranteed. In COLIBRE, the only free parameter in the star formation model is the fraction of gas mass converted into stars per free-fall time, provided the gas satisfies the instability criterion of Eq. 1. The adopted value is taken from observations of local universe molecular clouds (e.g. Schinnerer & Leroy 2024) rather than to ensure agreement with the observed KS relation, and it does not know how much H I or H_2 a gas particle has. The latter can then lead to large variations in the KS law with gas metallicity for example, which we return to in § 3.2.1.

The predictions of COLIBRE presented here agree with those in Nobels et al. (2024) at $\log_{10}(\Sigma_{H_2}/M_\odot\,pc^{-2}) \gtrsim 0.5$. At lower values, the simulation results in Nobels et al. (2024) drop towards longer depletion times. COLIBRE instead tends to continue on the constant depletion time line or even flatten a bit towards shorter depletion times. This difference is not necessarily surprising as there are many components to the physical model of COLIBRE that were not present in Nobels et al. (2024), including the non-equilibrium chemistry component, live dust and chemical evolution model and the overall cosmological context, which is lacking in Nobels et al. (2024). Regarding the non-equilibrium chemistry, by applying Chimes to the FIRE simulations, Richings et al. (2022) show that explicitly solving for the chemistry of the gas leads to varying H I and H_2 mass fractions at low densities ($n_H \lesssim 1\,cm^{-3}$), which will then change the relation between SFR and H I or H_2 in that regime. In the future, we will quantify the effect the different subgrid physics modules and parameters have on the KS relation and its scatter.

To understand what gives rise to the different relations between Σ_{SFR} and the H I and H_2 gas content, it is informative to study where these gas phases are located in the phase-space diagram. We show this in Fig. 3 for galaxies with stellar masses $> 10^9\,M_\odot$ and SFR > 0. From the H I distribution we see the bimodality that arises from H I being primarily in the WNM and CNM (see Eq. 2) of the ISM. Most of the H I mass is however contributed by the WNM ($\approx 64\%$). For H_2, we see that very little is in the WNM, with most of it being in the CNM ($\approx 99\%$). Note, however, that most of the gas mass in the CNM is atomic ($\approx 70\%$), while only $\approx 30\%$ is molecular. For the SFR, we see that $\approx 7\%$ is associated with the WNM and 93% with the CNM.

Even though most of the CNM consists of atomic rather than molecular gas, the correlation of the SFR is stronger with H_2 than H I or total neutral gas (as seen by the smaller scatter of the H_2). The reason for this is that even within the CNM, the densities traced by H_2 and SFR are much higher than those traced by the HI. This is shown in Fig. 4 for the L200m6 and L025m5 simulations. Even in comparison to H_2, the SFR is concentrated in higher density

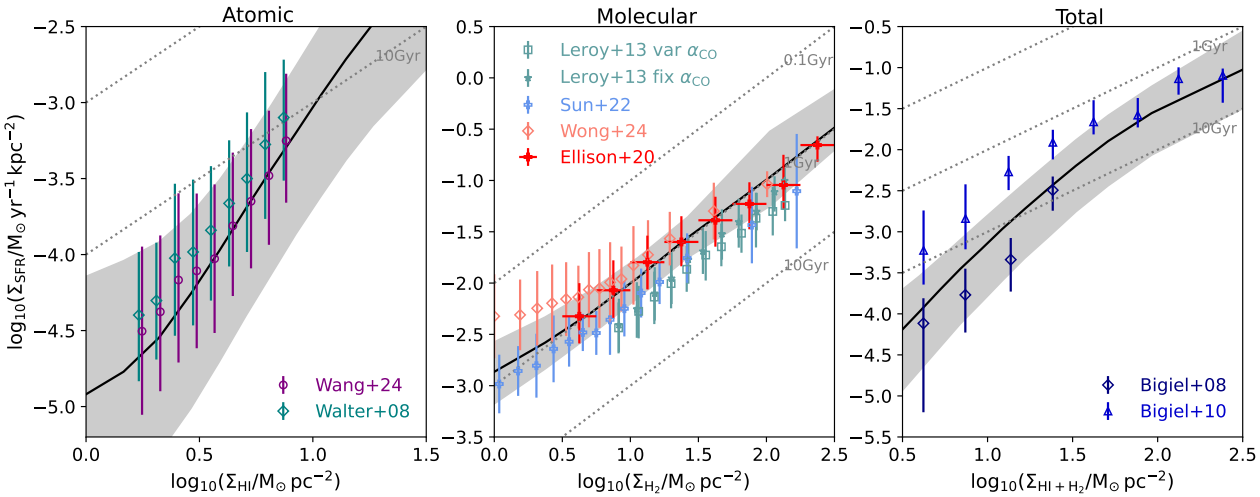

Figure 2. KS relation for H I (left panels), H_2 (middle panels) and total neutral hydrogen (H I+H_2) (right panels) for galaxies at $z = 0$ with $M_\star \geq 10^9\,M_\odot$ in the COLIBRE simulation L200m6 (see Table 1). The KS relations are calculated as azimuthal averages in rings with a width of 1 kpc. Black lines and shaded regions show the median and $16^{th} - 84^{th}$ percentile ranges, respectively, for COLIBRE. The bins are chosen to have a similar number of rings per bin, and always ≥ 10. For reference we show in each panel dotted lines of constant gas depletion time (0.1, 1 and 10 Gyr), as labelled. We show observations from Walter et al. (2008); Wang et al. (2024) for HI, Leroy et al. (2013); Ellison et al. (2020); Sun et al. (2022); Wong et al. (2024) for H_2 and Bigiel et al. (2008, 2010) for total neutral gas, as labelled in each panel. For Leroy et al. (2013) we show two sets of values, using a constant and a variable CO-to-H_2 conversion factor (α_{CO}) to demonstrate the typical level of systematic uncertainty introduced by this conversion. Note that the x- and y-axes ranges are different in each panel and chosen to span the range over which observations are reported.

gas regardless of the resolution. Thus, the larger fraction of SFR associated with the high-density tail of the CNM, where the H_2 resides is the cause of the stronger correlation between Σ_{SFR} and Σ_{H_2} than between Σ_{SFR} and Σ_{HI} or Σ_{HI+H_2} . Comparing the m5 and m6 curves, we see that the SFR-weighted density distribution moves to higher values as the resolution increases. This is because the criterion for gravitational instability is evaluated at the resolution limit. The H I- and H_2-weighted distributions also move to higher densities, but to a lesser extent than the SFR-weighted gas density distribution.

Fig. 3 shows a population of particles with SFR > 0 and $T \approx 10^4$ K, which is neither associated with significant H_2 nor HI. These particles correspond to those that were evaluated to have non-zero star formation rate at the beginning of the timestep, but received energy from stellar feedback at the end of the timestep. This is a rare occurrence and these particles contribute only $\approx 0.7\%$ to the total instantaneous SFRs of galaxies in our sample. In any case, the star formation model in COLIBRE is such that these particles would not turn into stellar particles because they would be classified as non star-forming at the beginning of the next timestep.

3.2 KS relation: characterising the scatter

3.2.1 Dependence on resolved galaxy properties

The KS relation predicted by COLIBRE and in the observations has a significant scatter. In this section we explore how the scatter is correlated with other resolved properties of galaxies, which were calculated using the particles tagged to belong to the same annuli in the ANNULI-FACE method.

Fig. 5 shows how the scatter in the KS relation at $z = 0$ for HI, H_2 and total neutral hydrogen depends on the stellar surface density (top), gas metallicity (middle) and dust surface density (bottom). Overall, we find that in all gas phases, the scatter around the KS relation tends to decrease with increasing gas density, even for HI. However, the decrease is stronger for H_2 and total neutral gas.

For $\Sigma_\star$ (top panels in Fig. 5), we find that as $\Sigma_\star$ decreases, the local H_2 depletion time, computed as $\Sigma_{H_2}/\Sigma_{SFR}$ decreases, which is clear at $\Sigma_{H_2} \lesssim 10\,M_\odot\,pc^{-2}$. At higher H_2 surface densities, there is little dependence of the H_2 KS relation's scatter on $\Sigma_\star$ For HI, lower $\Sigma_\star$ are associated with lower HI-to-SFR conversion efficiencies at fixed Σ_{HI}, opposite to the trend displayed in the H_2 case. The trend between the KS relation scatter and $\Sigma_\star$ at fixed gas surface density appears stronger for H I than H_2. We will come back to this point later. The total neutral gas appears similar to what is observed for the H I KS relation. This is not surprising as at $z = 0$ the overall gas content of galaxies tends to be dominated by H I rather than H_2.

For the gas metallicity (i.e. metals not locked in dust; middle panels in Fig. 5), we see again opposite trends in H I and H_2, the lower metallicity gas tends to be associated with a higher (lower) conversion efficiency between H_2 (H I) and stars. The dust surface density trends (lower panels in Fig. 5) resemble those of the gas metallicity: lower Σ_{dust} is associated with more (less) efficient conversion from H_2 (H I) into stars.

The physical drivers of the relations between the scatter of the KS relation and the gas metallicity and dust content are the same. As the gas becomes more metal and dust poor, it needs to reach higher densities for it to be cold and hence likely to form stars. In the absence of dust (or at least if it is scarce), the cold, dense gas will struggle to form H_2. Hence, as the gas becomes more metal and dust-poor, less H_2 and more H I are associated with the same amount of SFR, leading to the appearance of a higher SFR conversion efficiency for H_2, and a lower one for HI. Orr et al. (2018) found a similar tendency for low-metallicity gas to be associated with longer depletion timescales for the total H I+H_2 KS relation in the FIRE simulations. They did not however explore the effect of gas metallicity on the H I and H_2 KS relation separately, partially because their model does not explicitly follow the formation of hydrogen species.

We show how the gas metallicity influences the H I and H_2 composition of the CNM in COLIBRE in Fig. 6. The H I mass fraction

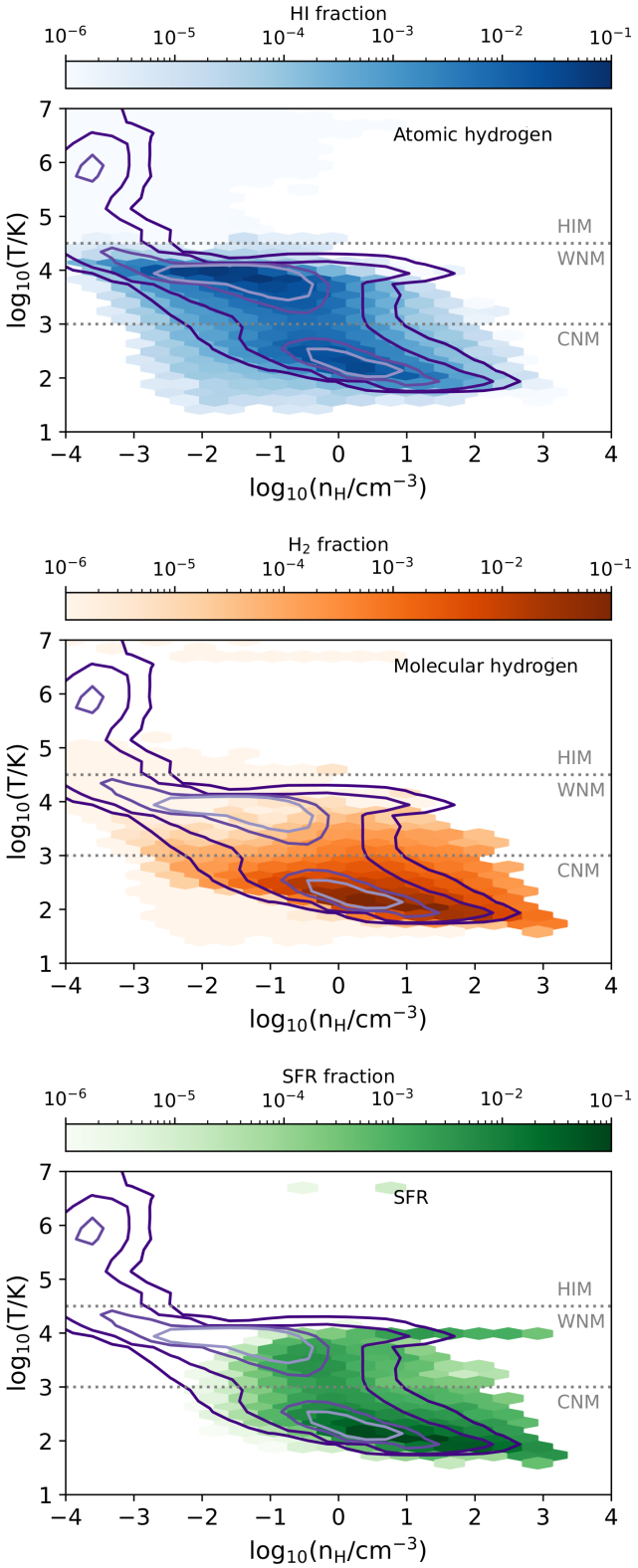

Figure 3. The distribution of all gas particles within 50 pkpc of the centre of mass of galaxies at $z = 0$ with $M_\star \geq 10^9\,M_\odot$ and SFR > 0 in the temperature-density plane. Contours enclose the regions where 99%, 95%, 68% and 50% of the particles are. The coloured hexbins show the H I (top), H_2 (middle) and SFR (bottom) contribution from each bin to the total HI, H_2 and SFR, respectively. The totals are obtained by summing these quantities of all the galaxies. The horizontal dotted lines mark the regions associated with the hot ionised (HIM), warm neutral (WNM) and cold neutral (CNM) media, as labelled, and as defined in Eq. 2.

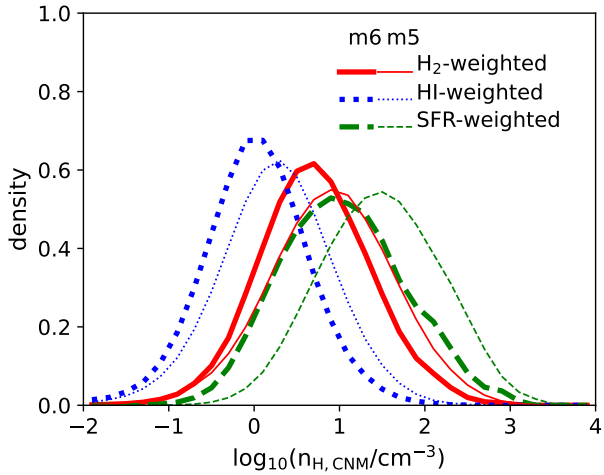

Figure 4. Probability density function of the gas density of gas particles in the CNM (as defined in Eq. 2), weighted by the H_2, H I mass or the SFR, as labelled. This is shown for $z = 0$ for gas particles in the L200 m6 (thick lines) and L025m5 (thin lines) simulations, that are in the CNM of galaxies at $z = 0$ with $M_\star \geq 10^9\,M_\odot$ and SFR> 0.

in the CNM saturates at ≈ 0.75 at low metallicity, as the rest of the gas is in helium and metals. The figure shows that the dependence of the H I fraction in the CNM on gas metallicity is qualitatively the same in the L200m6 and the L025m5 simulations, showing that the result is robust against resolution. We also show the typical gas density at which stars form in COLIBRE for the m6 and m5 resolution. At m6 resolution, the density consistently decreases with decreasing metallicity, even dropping below $n_H \approx 1\,cm^{-3}$ for the very metal-poor gas. This is, however, driven by resolution, as for the m5 run we see that star formation consistently happens at densities $> 10\,cm^{-3}$, even when H I overwhelmingly dominates the mass of CNM. We remind the reader that this difference between resolutions is expected and intentional, as the instability criterion for star formation is evaluated at the resolution limit. At the Milky-Way metallicity of $12 + \log_{10}(O/H) \approx 8.75$, COLIBRE predicts the fraction of H I in the CNM to be ≈ 0.5, which is similar to the value observed in the Milky-Way (McClure-Griffiths et al. 2023). This is indicative only, as we are not selecting galaxies to be of Milky-Way mass in Fig. 6. At lower metallicities, Park et al. (2025) find that there is more H I in the CNM, which they interpret as the gas remaining H I as it gets colder due to the difficulty in forming H_2 in the absence of dust. This is in qualitative agreement with what Fig. 6 shows for COLIBRE.

Fig. 7 explores the strength of the correlations between the gas depletion time, measured in a spatially resolved manner, $\tau_{gas} \equiv \Sigma_{gas}/\Sigma_{SFR}$, and the resolved properties in galaxies (including those shown in Fig. 5). To show all the correlations together, we simply subtract from every property its corresponding median for the entire sample of Fig. 5. For example, for the stellar surface density, the x-axis shows $\log_{10}(\Sigma_\star) - \langle\log_{10}(\Sigma_\star)\rangle$.

For τ_{H_2}, we find that the strongest correlation is the negative correlation with specific Σ_{SFR} ($s\Sigma_{SFR}$; which is related to the correlation with $\Sigma_\star$), and slightly weaker positive correlations appears with Σ_{dust} and local gas metallicity. The strong anti-correlation between τ_{H_2} and resolved sSFR means that the high sSFR is not just due to a higher concentration of cold gas but also that the cold gas is being converted into stars more efficiently. In the case of the gas metallicity and dust surface density, the presence of a moderately strong correlation with τ_{H_2} is not unexpected, as the accumulation of metals and dust directly

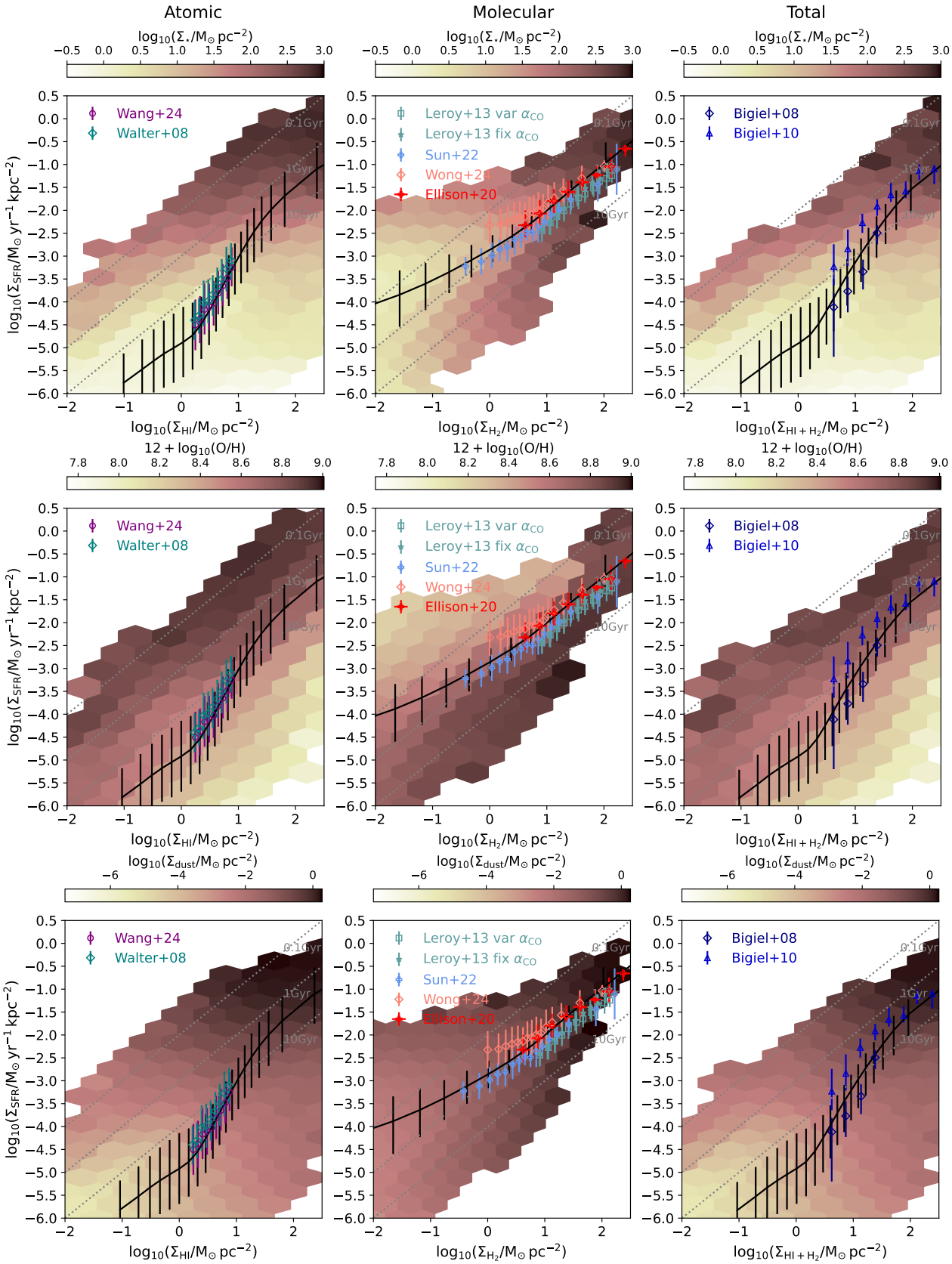

Figure 5. As Fig. 2 but with the coloured bins showing the median stellar surface density ($\Sigma_\star$; top panels), gas metallicity ($\log_{10}$(O/H); middle panels) and surface density of dust ($\Sigma_{\rm dust}$, lower panels). Black lines with error bars in each panel show the median and 16$^{\rm th}$ – 84$^{\rm th}$ percentile ranges, respectively. Only hexbins with $\geq$ 5 objects are included.

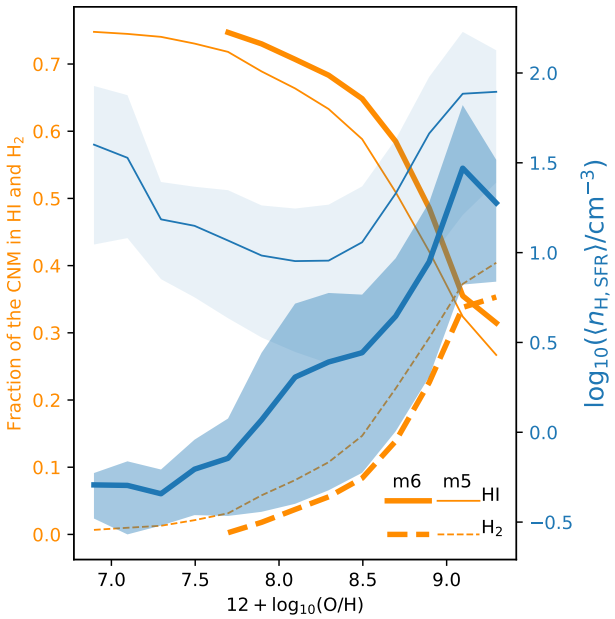

Figure 6. The fraction of the CNM in the form of H I (orange solid line) and H_2 (orange dotted line), and the SFR-weighted gas density (blue line with shaded region), as a function of gas metallicity. This is constructed with all the gas particles that are within 50 pkpc from the centres of galaxies with $M_\star \geq 10^9\,M_\odot$ and SFR > 0 at $z = 0$ in the L200m6 (thick lines) and L025m5 (thin lines) simulations. The H I fraction saturates at a CNM fraction of ≈ 0.75, as the rest of the gas is in the form of helium and metals. For the gas density, we show the median and the $16^{\rm th} - 84^{\rm th}$ percentile ranges.

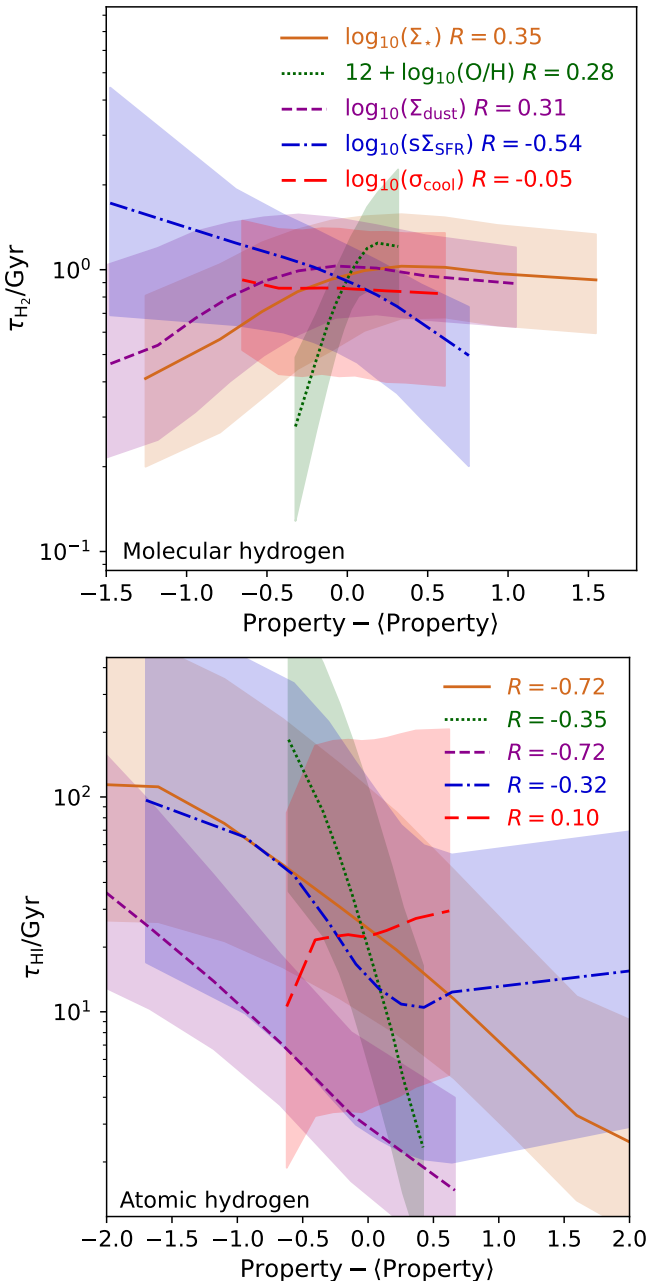

Figure 7. The correlation between the H_2 (top) and H I (bottom) depletion times, defined as $\Sigma_{\rm gas}/\Sigma_{\rm SFR}$, with gas being either H_2 or HI, and the stellar surface density, cold gas metallicity, surface density of dust, local sSFR and cool gas velocity dispersion (as defined in Eq. 3), as labelled. Lines and shaded regions show medians and $16^{\rm th} - 84^{\rm th}$ percentile ranges, respectively, for galaxies at $z = 0$ with $M_\star \geq 10^9\,M_\odot$. To plot all the properties on the same x-axis scale, we subtract from every property its median. We also show the Spearman correlation coefficient, R, of each correlation, as labelled.

affects the efficiency of gas cooling and H_2 formation, but the fact that the correlations are positive is more surprising. In COLIBRE, dust acts both as a catalyst for the formation of H_2 and helps shield the gas. In this case, more of the hydrogen gas is in the form of H_2 and thus associated with a given SFR, giving the appearance of a longer H_2 depletion time. We test these predictions against observations in § 3.2.3.

In the case of $\tau_{\rm HI}$ (bottom panel in Fig. 7), we find that the strongest correlations are with the dust and stellar surface densities (both with a Spearman correlation coefficient ≈ -0.75). The latter dependence has also been reported in observations; e.g. Wang et al. (2024) find $\tau_{\rm HI} \propto \Sigma_\star^{-0.85\pm0.09}\Sigma_{\rm SFR}/\Sigma_{\rm HI}$. In COLIBRE, we find $\tau_{\rm HI} \propto \Sigma_\star^{-0.72}$, in relatively agreement with these observations (see § 3.2.3 for a more detailed comparison with Wang et al. 2024). The strong anti-correlation between $\tau_{\rm HI}$ and $\Sigma_{\rm dust}$ is expected. The more dust there is, the easier it is for the hydrogen to transition from atomic to molecular, resulting in a relative lower fraction of star formation associated with atomic hydrogen. This leads to an apparent higher efficiency of H I to SFR conversion.

Interestingly, the cool gas ($T < 10^{4.5}$ K) one-dimensional velocity dispersion (Eq. 3) is only weakly correlated with $\tau_{\rm HI}$, while the correlation with $\tau_{\rm H_2}$ is almost absent. Schaye et al. (2026) show that in COLIBRE, stars tend to form from cold gas with supersonic turbulent velocities. Our results show that, even though at the resolution limit the velocity dispersion (especially the turbulent component) play an important role in the star formation model, at kpc scales, star formation appears to be poorly correlated with gas velocity dispersion. We also tested different definitions of the gas velocity dispersion (weighting by H_2 or H I mass, and using different selections in distance from the midplane ranging from 3 to 10 kpc), and found that the weak correlation holds for different definitions.

The correlation with $\sigma_{\rm cool}$ manifests in a way that a higher velocity dispersion is associated with a longer H I depletion time. The star formation model in COLIBRE indirectly depends on the local gas velocity dispersion, since a higher value increases the Toomre instability parameter, making the gas less likely to collapse and be

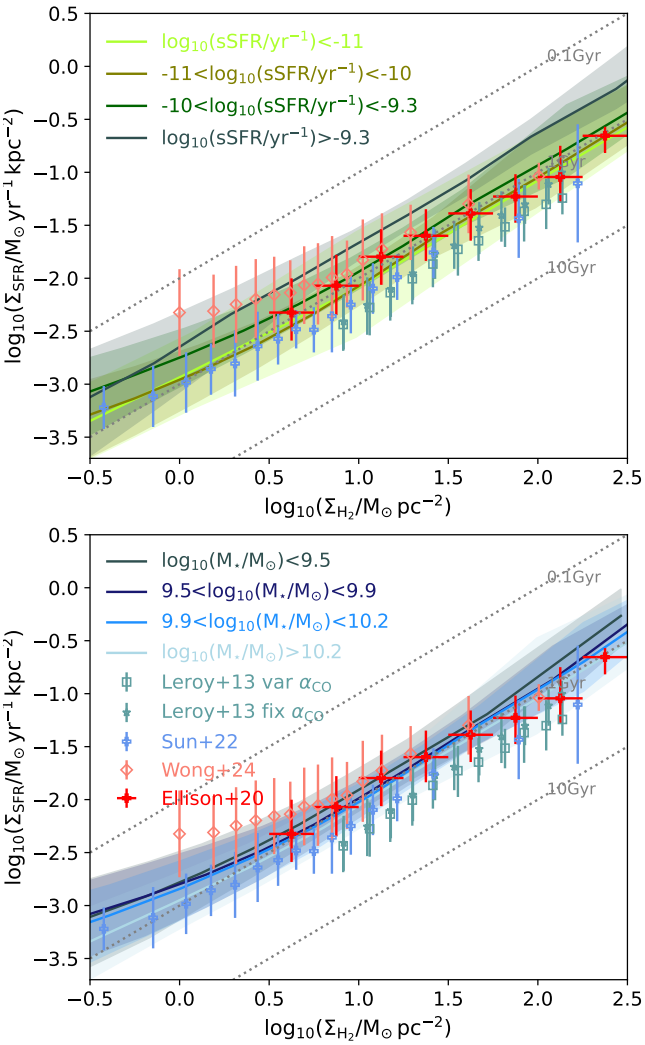

Figure 8. The H_2 KS relation at $z = 0$ for galaxies selected based on their sSFR (top panels) and stellar mass (bottom panel). The median and $16^{th} - 84^{th}$ percentiles are shown with solid lines and shaded regions, respectively. All galaxies included here have $M_\star \geq 10^9\,M_\odot$ and SFR > 0.

available for star formation (see Nobels et al. 2024 for a detailed discussion). The weaker correlation with σ_{cool} compared to some of the other local properties is in part due to σ_{cool} displaying less variations within and in-between galaxies, compared with other local properties. This is clear from the dynamic range covered by σ_{cool} which only extends over 1 dex, while $\Sigma_\star$, Σ_{dust} and $s\Sigma_{SFR}$ tend to display variations of $\gtrsim$ 1.5 dex within our sample. Note, however, that the gas metallicity also varies over a small range compared to some of the other properties, while still displaying stronger correlations with both τ_{H_2} and τ_{HI} than what is obtained for σ_{cool}.

The total neutral hydrogen (H I+H_2) behaves very much like τ_{HI}, with the correlations only becoming a bit weaker than what is reported in the bottom panel of Fig. 7. This simply means that H I dominates the neutral gas reservoir in most galaxies at $z = 0$ in COLIBRE.

In Appendix A, we test the convergence of the correlations in Fig. 7 with numerical resolution. We find that all correlations are very well converged between the m6 and m5 resolution, with the exception being the correlation between τ_{H_2} and local gas metallicity. Although the correlation is similarly strong in the L025m5 compared to the L025m6 simulation (see Table A1), there is an offset in normalisation. This is not surprising given that the stellar mass-gas metallicity relation is not well converged in COLIBRE at $z = 0$ (see discussion in Schaye et al. 2026).

3.2.2 *Dependence on global galaxy properties*

Fig. 8 presents the molecular gas KS relation at $z = 0$, separating the galaxy population by their global sSFR (top) and stellar mass (bottom). We show these properties because they are the ones that exhibited the strongest correlations with the scatter of the KS relation. In addition to the trends in Fig. 8, we also explored a possible dependence of the KS relation scatter on global gas metallicity, stellar age, galaxy type (whether the galaxies are defined as central or satellites) and galaxy morphology, and found only weak or no correlations.

The top panel of Fig. 8 shows a strong dependence of the molecular KS relation's normalisation on the global sSFR of the galaxy, in a way that galaxies with higher sSFR have shorter molecular gas depletion times. COLIBRE galaxies can have high sSFRs from a combination of increased gas reservoirs and a more efficient conversion of cold gas into stars. We quantify this effect by measuring the Spearman correlation coefficient R, between the resolved molecular depletion time and the global sSFR, at fixed global molecular and stellar masses. We find $R \approx -0.6$ with negligible p-values, indicating strong anti-correlations. The dependence across bins of stellar and molecular gas masses is similar and takes the shape $\tau_{H_2} \propto \mathrm{sSFR}^\beta$, with $\beta \approx [-0.8, -0.9]$. Thus, COLIBRE predicts that changes in the global sSFR are accompanied by changes in the local conversion efficiency of molecular gas to stars.

The bottom panel of Fig. 8 shows a weak dependence on stellar mass, so that lower stellar mass galaxies have slightly elevated Σ_{SFR} at fixed Σ_{H_2}, with the differences being more clearly seen at $\Sigma_{H_2} \gtrsim 10\,M_\odot\,pc^{-2}$. We find that the dependence on stellar mass in the bottom panel of Fig. 8 is driven by the sSFR dependence, as the sSFR has a negative dependence on stellar mass for main sequence galaxies (see Fig. 16 in Schaye et al. 2026).

3.2.3 *Comparison with observations*

In this section, we present a series of comparisons between the predicted dependence of the scatter in the KS relation on galaxy properties, starting with the atomic gas and then moving to the molecular gas. Because most observational constraints are dedicated to the molecular KS relation, this section is devoted primarily to that.

Shi et al. (2011) showed that there is a strong dependence of the scatter in the atomic gas KS relation on the stellar surface density, suggesting that it could be fundamentally driven by the dynamical equilibrium pressure. We compare the predicted relation between the local H I depletion time ($\equiv \Sigma_{HI}/\Sigma_{SFR}$) and the local stellar surface density with observations in Fig. 9. We show observations from the FEASTS (Wang et al. 2024) and PHANGS (Sun et al. 2022) surveys. FEASTS comprises 17 spiral galaxies with stellar masses $10^{9.7} - 10^{11}\,M_\odot$, while PHANGS contains 70 nearby galaxies with stellar masses between $10^9 - 10^{11}\,M_\odot$. In both observational sets, the relation was computed using radial annuli with size $\approx$ 1 kpc, similar to our method. The agreement between COLIBRE and the observations is excellent, even when we did not attempt to match the exact distribution of galaxy properties of the two surveys and limited to sampling a similar stellar mass range. This relation is very well converged with resolution, as shown in Fig. A3, so the agreement extends to the other COLIBRE simulations.

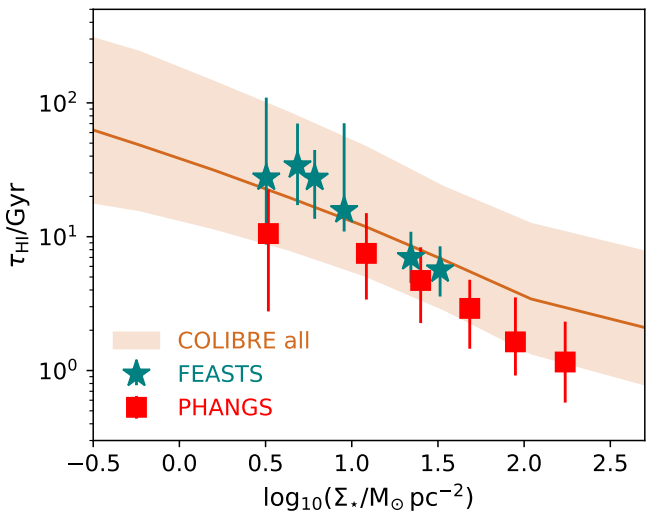

Figure 9. The dependence of the (resolved) H I depletion time, $\tau_{\rm HI}$ on the local stellar surface density, $\Sigma_\star$, for COLIBRE galaxies at $z = 0$ with $M_\star \geq 10^9\,{\rm M}_\odot$ compared with the FEASTS (Wang et al. 2024) and PHANGS (Sun et al. 2022) surveys. The lines and symbols show the median of COLIBRE and the observations, respectively, while the shaded region and error bars show the $16^{\rm th} - 84^{\rm th}$ percentile ranges. This threshold matches well the minimum $\Sigma_{\rm HI}$ value in FEASTS and PHANGS.

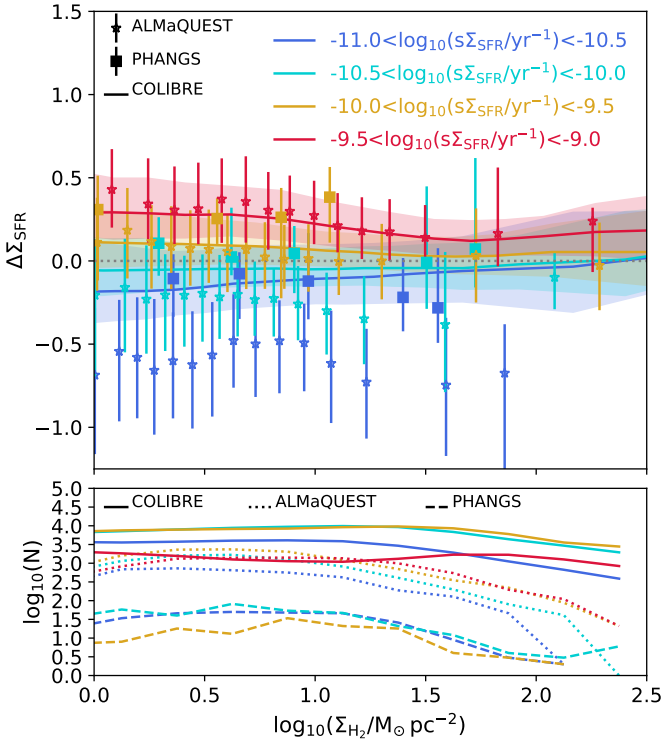

Figure 10. *Top panel:* Deviations from the median molecular gas KS relation ($\log_{10}(\Sigma_{\rm SFR}) - \langle\log_{10}(\Sigma_{\rm SFR})\rangle$) at $z = 0$ as a function of H_2 surface density, separating regions by their local sSFR ($s\Sigma_{\rm SFR} \equiv \Sigma_{\rm SFR}/\Sigma_\star$, for observations (symbols) and COLIBRE (lines). Symbols and lines show medians, while error bars and shaded regions show the $16^{\rm th} - 84^{\rm th}$ percentile ranges. For ALMaQUEST (Lin et al. 2019), we include all galaxies and spaxels; for PHANGS (Sun et al. 2022), we include all galaxies and annuli; while for COLIBRE we include $z = 0$ galaxies with $M_\star > 10^{9.7}\,{\rm M}_\odot$ and SFR > 0. Note that no PHANGS data are presented for the highest $s\Sigma_{\rm SFR}$ bin, as there were not enough statistics to produce reliable measurements for the medians and scatter. The agreement between COLIBRE and the observations is remarkable. At low values of sSFR, COLIBRE agrees better with PHANGS. *Bottom panel:* histogram of $\Sigma_{\rm H_2}$ for each of the samples of the top panel. The observational and simulated samples follow similar distributions, with most regions having $\log_{10}(\Sigma_{\rm H_2}/{\rm M}_\odot\,{\rm pc}^{-1}) \lesssim 1.4$. This is also the regime in which the differences between sSFR samples are clearest in both observations and simulations.

As shown in Fig. 7, $\Sigma_\star$ is one of the most significant drivers of the scatter in the H I KS relation in COLIBRE, and the same appears to be the case in the observations. It is important to note that FEASTS appears to be slightly elevated compared to PHANGS, while COLIBRE lies in between. This most likely comes from the diffuse H I FEASTS is sensitive to (due to the data coming from the single dish Five-hundred-meter Aperture Spherical Telescope), but that PHANGS misses (as it primarily employs the interferometric Very Large Array). According to Wang et al. (2024), diffuse H I can account for up to 40% of the H I mass, which directly translates into increasing $\tau_{\rm HI}$ in a direct proportion. In COLIBRE, the local dynamical equilibrium pressure does not enter the star formation model, implying that the $\tau_{\rm HI} - \Sigma_\star$ correlation does not necessarily directly emerge from that parameter.

The scatter of the molecular gas KS relation in galaxies in the local Universe has been well studied with the ALMaQUEST (Lin et al. 2019), EDGE-CALIFA (Wong et al. 2024) and PHANGS (Sun et al. 2022) surveys. Here, we compare our predictions in detail with ALMaQUEST and PHANGS. The ALMaQUEST sample consists of 46 galaxies with stellar masses $10^{9.7} - 10^{11.5}\,{\rm M}_\odot$, with 25 of those being on the main sequence and 21 being below the main sequence (referred to as "Green Valley" galaxies). Via a combination of MaNGA and ALMA CO(2-1) observations, they characterise the SFR, molecular gas, stellar surface density and gas metallicity of individual spaxels in galaxies, with spaxels having sizes of 0.3 kpc. The PHANGS sample with H_2 profile measurements consists of 61 galaxies (stellar mass range is as indicated above), and here we use the data provided in annuli of 1 kpc width from Sun et al. (2022). Using the same sSFR criterion as Lin et al. (2019), the PHANGS catalogue consists of 19 main sequence and 45 Green Valley galaxies, thus PHANGS samples lower sSFR galaxies than ALMaQUEST on average. Another important difference between PHANGS and ALMaQUEST is that the SFRs of the regions in PHANGS are characterised using a combination of Hα, FUV, NUV and MIR, while in ALMaQUEST they come only from Hα.

Although PHANGS extends to lower stellar masses compared with ALMaQUEST, most galaxies (54/61) have masses $\gtrsim 10^{9.8}\,{\rm M}_\odot$. Thus, to compare with observations, we select galaxies in COLIBRE at $z = 0$ that have stellar masses $> 10^{9.7}\,{\rm M}_\odot$ and SFR > 0. We choose a slightly lower stellar mass limit than the minimum mass of the ALMaQUEST sample to allow for potential systematic uncertainties in the derivation of stellar masses of the order of those inferred at $z = 0$ (Bellstedt & Robotham 2024). To perform the comparison with observations, we define $\Delta\,\Sigma_{\rm SFR} \equiv \log_{10}(\Sigma_{\rm SFR}) - \langle\log_{10}(\Sigma_{\rm SFR}(\Sigma_{\rm H_2})\rangle$, where $\Sigma_{\rm SFR}$ corresponds to the value of an annulus (or spaxel in the case of ALMaQUEST) and $\langle\log_{10}(\Sigma_{\rm SFR}(\Sigma_{\rm H_2})\rangle$ corresponds to the median of all annuli (or spaxels) within a bin of $\Sigma_{\rm H_2}$. We calculate this quantity for both simulation and observations, which helps us to focus on how the scatter of the relation correlates with properties of interest.

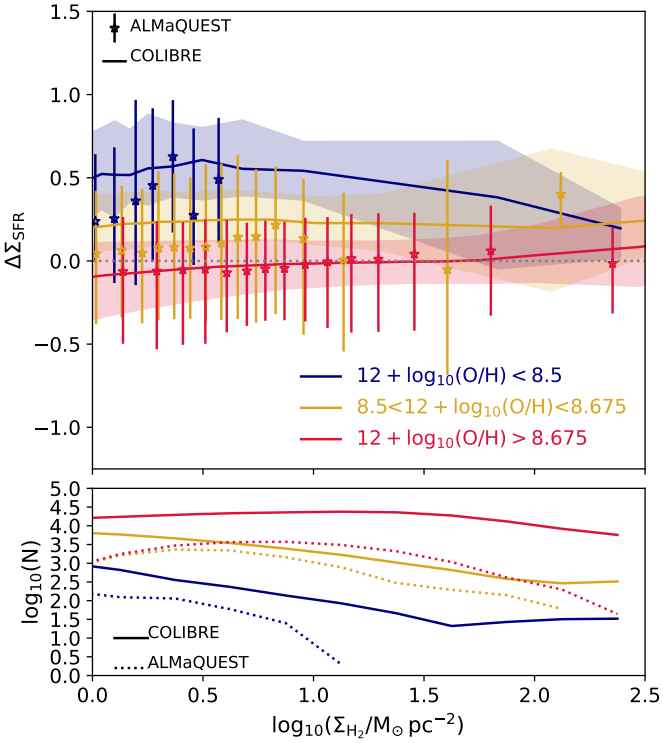

Figure 11. As Fig. 10 but for regions binned by the local gas metallicity, $12 + \log_{10}(\mathrm{O/H})$, and comparing only with ALMaQUEST. The sampling of the metallicity bins is similar in both observations and simulations, with a similar distribution of $\log_{10}(\Sigma_{\mathrm{H_2}}/\mathrm{M_\odot\,pc^{-1}})$ in each metallicity bin.

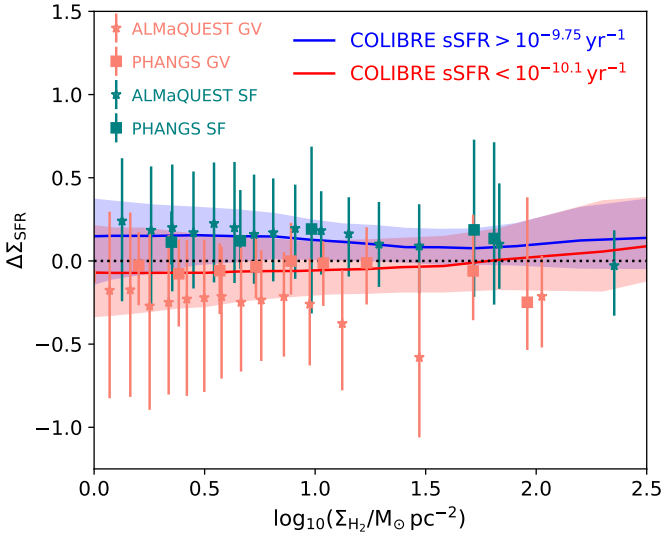

Figure 12. As the top panel of Fig. 10, but for star-forming and green-valley galaxies separately, in COLIBRE (lines) and observations (symbols), as labelled. This is shown for galaxies at $z = 0$. Symbols and lines show medians, while error bars and shaded regions show the $16^{\mathrm{th}} - 84^{\mathrm{th}}$ percentile ranges. To select the two samples in COLIBRE, we apply thresholds in sSFR, as labelled, which give median sSFR similar to the median sSFR in ALMaQUEST and PHANGS for the two samples. The agreement between COLIBRE and the observations is very good, particularly when comparing with PHANGS.

We start by comparing the resolved dependence of the scatter of the molecular KS relation on the sSFR in Fig. 10. Here, we take all $z = 0$ galaxies in COLIBRE with stellar masses $> 10^{9.7}\,\mathrm{M_\odot}$, and simply bin annuli by their local $\mathrm{sSFR} \equiv \Sigma_{\mathrm{SFR}}/\Sigma_\star$. COLIBRE predicts a very strong dependence of the scatter in the molecular KS relation on the local sSFR that agrees remarkably well with the observed dependence in ALMaQUEST at $\mathrm{sSFR} > 10^{-10}\,\mathrm{yr^{-1}}$, which better samples the high $\mathrm{s}\Sigma_{\mathrm{SFR}}$ region. At lower sSFR values, we see that ALMaQUEST displays a lower normalisation of the KS relation than predicted by COLIBRE, while there is excellent agreement with PHANGS. This may be related to ALMaQUEST using Hα to derive SFRs, which is known to systematically underestimate SFRs compared to UV/IR tracers at low SFRs (Lee et al. 2009). PHANGS on the other hand, by using a combination of tracers, circumvents this limitation.

We remind the reader that beyond the local sSFR, the scatter of the molecular KS relation is correlated with the local gas metallicity (Fig. 7). We test this prediction with ALMaQUEST only, as the data for the metallicity profiles for PHANGS were not available (see Sun et al. 2022 for details). Fig. 11 shows $\Delta\,\Sigma_{\mathrm{SFR}}$ as a function of $\Sigma_{\mathrm{H_2}}$ for samples selected by local gas metallicity. To build Fig. 11, we removed all spaxels in the ALMaQUEST sample that have too low signal-to-noise ratio ($\mathrm{S/N} < 3$) to measure a gas metallicity, which removes 17% of the spaxels. The removed spaxels tend to be those with long $\mathrm{H_2}$ depletion times. Thus, the resulting sample tends to be biased towards short depletion times and high $\Sigma_{\mathrm{H_2}}$ (see the bottom panel of Fig. 11) compared to what is seen in the bottom panel of Fig. 10. Despite these differences, we see a similar trend in COLIBRE and ALMaQUEST: $\Delta\,\Sigma_{\mathrm{SFR}}$ decreases as the gas metallicity increases. This is particularly clear in the $0.25 \lesssim \log_{10}(\Sigma_{\mathrm{H_2}}/\mathrm{M_\odot\,pc^{-2}}) \lesssim 0.75$ range that is best sampled by the observations.

We stress that from the ALMaQUEST sample alone, it is not clear whether gas metallicity is more weakly or strongly correlated with $\tau_{\mathrm{H_2}}$ than other properties are. This could in part be due to the large fraction of spaxels we need to remove from the sample due to the low signal-to-noise ratio, but also to the limited stellar mass range of the sample, which is skewed towards massive galaxies. The mass-metallicity relation is steep at $M_\star \lesssim 10^{10}\,\mathrm{M_\odot}$ but flattens at higher stellar masses (e.g. Tremonti et al. 2004). Hence, the overall metallicity range sampled by ALMaQUEST is rather small, with 90% of the spaxels having $8.57 < 12 + \log_{10}(\mathrm{O/H}) < 8.8$. Future surveys sampling a larger dynamic range in gas metallicity would be needed to test the relative importance of different properties in setting the scatter of the molecular KS relation.

For the comparison above, we used all spaxels in ALMaQUEST and all annuli in PHANGS regardless of whether galaxies were classified as star-forming or green valley, and only investigated the dependence of the scatter in the molecular KS relation on resolved properties. Lin et al. (2022) argue that global galaxy properties also impact the resolved KS relation, and find that green-valley galaxies in ALMaQUEST have a lower global molecular-to-star formation conversion efficiency than star-forming galaxies. In Fig. 12, we compare with those results by splitting our COLIBRE sample into star-forming and green valley galaxies, in such a way that the median sSFR of each sample resembles that of ALMaQUEST and PHANGS. We find that a selection $\mathrm{sSFR} > 10^{-9.75}\,\mathrm{yr^{-1}}$ in COLIBRE provides a median $\mathrm{sSFR} \approx 10^{-9.64}\,\mathrm{yr^{-1}}$ while the median for the star-forming samples in ALMaQUEST and PHANGS is $\mathrm{sSFR} \approx 10^{-9.65}\,\mathrm{yr^{-1}}$ and $\approx 10^{-9.7}\,\mathrm{yr^{-1}}$, respectively. We select green-valley galaxies in COLIBRE to have $\mathrm{sSFR} < 10^{-10.1}\,\mathrm{yr^{-1}}$, which produces a sample with a

median sSFR $\approx 10^{-10.65}$ yr^{-1}, while the green-valley ALMaQUEST and PHANGS samples have medians of sSFR $\approx 10^{-10.57}$ yr^{-1} and $\approx 10^{-10.45}$ yr^{-1}, respectively. We remind the reader that in COLIBRE, annuli are selected to have SFR > 0. We find excellent agreement between the molecular KS relation in COLIBRE with both sets of observations for the SF galaxies, while for green-valley galaxies, the agreement is better with PHANGS. The latter resembles the findings of Fig. 10, where the Hα-derived SFRs at low sSFR in ALMaQUEST appear to underestimate the SFR values compared to the multi-wavelength approach of PHANGS.

The comparisons presented in Figs. 2, 10, 11 and 12 show that COLIBRE predicts a resolved KS relation at $z = 0$ in different gas phases in excellent agreement with the observations. This is not only the case for the average relation, but also for the dependence of the KS relation's scatter on local and global galaxy properties. This is a remarkable success, as the KS relation was not used to calibrate the free parameters in COLIBRE.

3.3 KS relation: galaxy-to-galaxy variations

We have explored the median KS relation and how the scatter correlates with resolved and global galaxy properties. In this section, we explore how much variation there is in the KS relation from galaxy to galaxy at $z = 0$. To quantify this, we fit the relationship between $\Sigma_{\rm SFR}$ and $\Sigma_{\rm gas}$, with gas here being HI, H_2 or the sum of the two, using the function:

$$\Sigma_{\rm SFR} = A_0\, \Sigma_{\rm gas}^{N_{\rm KS}} \tag{4}$$

In this equation, $\Sigma_{\rm SFR}$ and $\Sigma_{\rm gas}$ take the units M$_\odot$ yr^{-1} kpc^{-2} and M$_\odot$ pc^{-2}, respectively. The fits for COLIBRE are performed using only gas with a surface density ≥ 0.1 M$_\odot$ pc^{-2}. This is done to avoid the flattening of the KS relation at lower surface densities due to resolution limitations (see Fig. A1) and to focus on regions that are directly comparable with observations. We do not see large variations in the individual fits as long as they are performed with a minimum surface density in the range $0.1 - 1$ M$_\odot$ pc^{-2}. In addition, we only fit galaxies with a KS relation sampled with ≥ 5 rings. This means that we do not fit some of the low SFR galaxies in COLIBRE. The example galaxy shown at the bottom-right panel of Fig. B1 has a well-defined fit for its H I KS relation, but not for the H_2 KS relation. We find that the requirement above removes 37% of the galaxies with $M_\star \geq 10^9$ M$_\odot$ and SFR > 0 at $z = 0$. The removed galaxies tend to have lower stellar masses and sSFRs (with medians $\approx 10^{9.48}$ M$_\odot$ and $\approx 10^{-10.17}$ yr^{-1}, respectively) than the ones that are kept for the analysis (with medians $\approx 10^{9.73}$ M$_\odot$ and $\approx 10^{-10.02}$ yr^{-1}, respectively). We tested different minimum numbers of bins between $3 - 7$ and found our results to be insensitive to that change.

Fig. 13 shows the correlations of $N_{\rm KS}$ and A_0 with stellar mass. For H I (blue), we find that the median slope of the entire population is $N_{\rm KS} \approx 2.15$, but the value of individual galaxies strongly anti-correlates with the stellar mass of the galaxy. Low-mass galaxies tend to have higher values of $N_{\rm KS}$, which is also seen for fits to the total gas (not shown here). The scatter around the median $N_{\rm KS}$ tends to increase with decreasing stellar mass for fits based on H I or total gas. For HI, the zero point of the KS fits is positively correlated with stellar mass. For the molecular gas, we see that the slope and the zero point are close to constant, with values ≈ 1 and ≈ -2.8, respectively (in the units used in Eq. 4). We also find virtually no difference between the different COLIBRE resolutions.

The number of fits to the observed KS relation of individual galaxies is limited to a few dozens, even in the local Universe. We show in

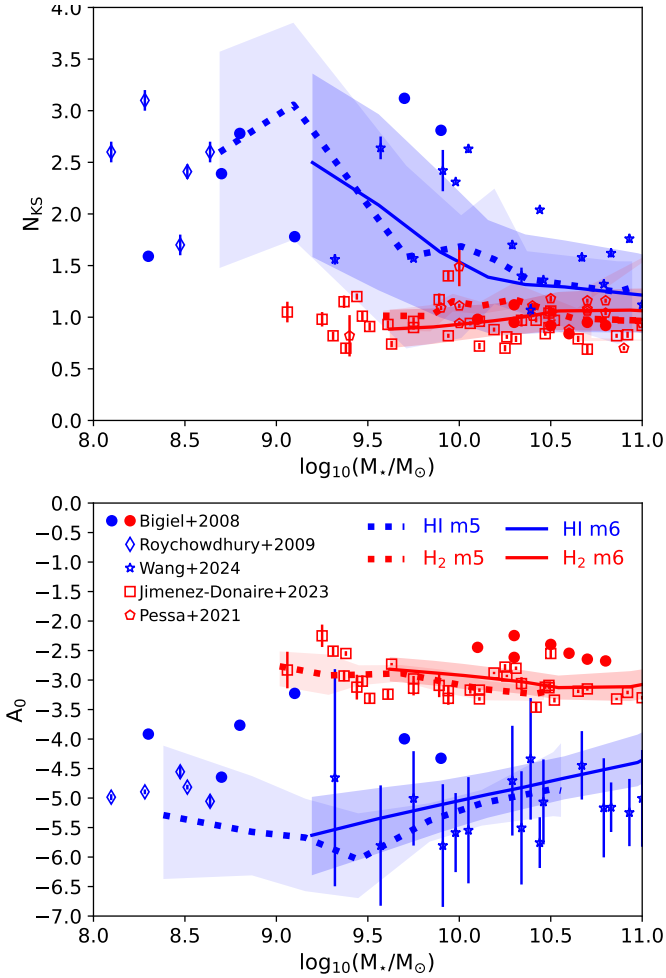

Figure 13. The slope (top) and zero-point (bottom) of the KS relation fits for individual $z = 0$ galaxies as a function of stellar mass in COLIBRE. We show results for the L200m6 (solid lines) and L025m5 (dotted lines) simulations, as labelled in the bottom panel. The equation being fitted is Eq. 4. We show the slope and zero-point of the fits for the case of fitting only H I (blue) and H_2 (red). Lines with shaded regions show the median and the 16$^{\rm th}$ – 84$^{\rm th}$ percentile ranges, respectively. Observational estimates from Bigiel et al. (2008); Roychowdhury et al. (2009); Pessa et al. (2021); Jiménez-Donaire et al. (2023); Wang et al. (2024) are shown as symbols, as labelled in the bottom panel, using the same colour-code of COLIBRE.

Fig. 13 observational results from different surveys, which agree on a close to constant KS molecular gas relation. We highlight that the observations of Jiménez-Donaire et al. (2023) correspond to Virgo cluster galaxies, with some of them being gas-deficient and clearly affected by their environment. Nevertheless, they follow a very similar relation. It is notable that the observations suggest a similar scatter in the slope and zero point of the molecular KS relation, as predicted by COLIBRE. The overall trends seen, including a potential weak dependence on stellar mass, also agree well with COLIBRE's predictions.

For HI, we again see very good agreement between the m5 and m6 resolutions. We note that the difference in A_0 for the H I KS relation between the L200m6 and L025m5 runs at around $M_\star \approx 10^{9.5}$ M$_\odot$ is driven by the different box sizes, as the differences become negligible when we compare the L025m5 simulation with the L025m6 simula-

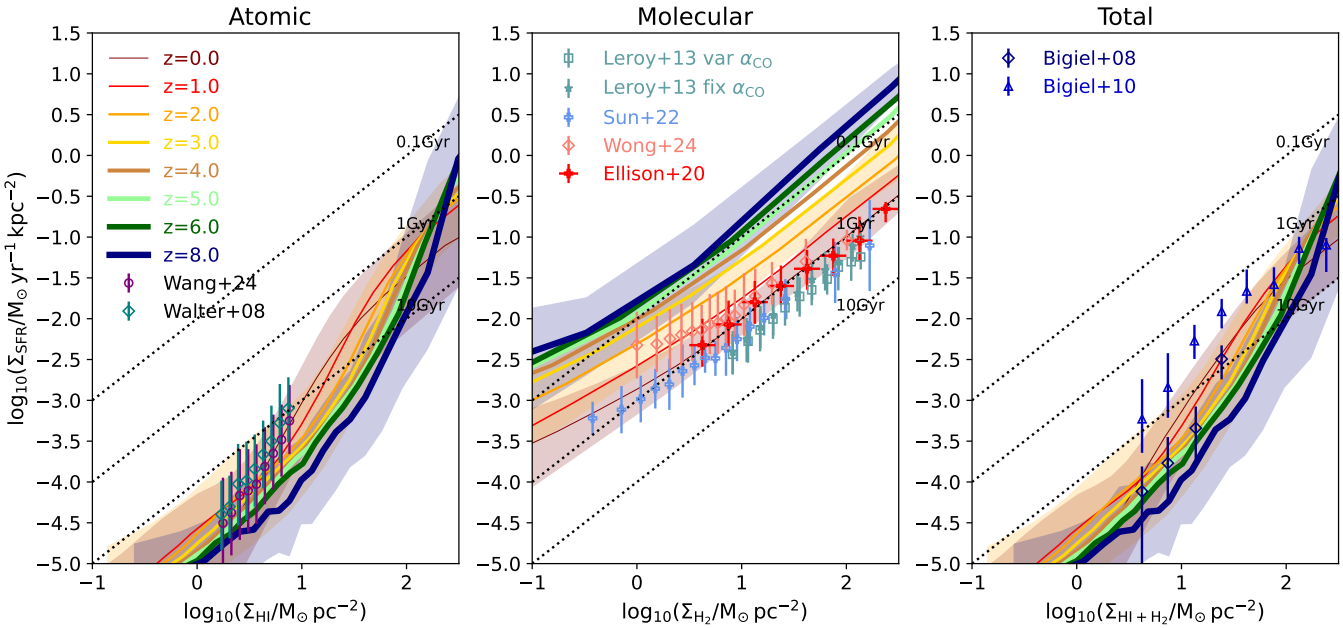

Figure 14. As Fig. 2 but showing the evolution of the median KS relation for galaxies with $M_\star \geq 10^9\,M_\odot$ and SFR > 0 from $z = 8$ to $z = 0$. We show the $16^{th} - 84^{th}$ percentiles only for $z = 0$, 2 and 8 for clarity. Redshifts are as labelled in the left panel. The observational data shown in all panels corresponds to $z \approx 0$.

tion instead of L200m6 (not shown here). It is informative to show the L025m5 run along with the L200m6 run as the observational fits to the H I KS relation are biased towards dwarf galaxies, which are H I dominated, and better resolved in the m5 run. To compare COLIBRE with observations, we compiled data from Bigiel et al. (2008); Roychowdhury et al. (2009); Wang et al. (2024). Roychowdhury et al. (2009) did not report stellar masses for their sample of dwarf galaxies, and hence we computed our own stellar masses from IRAC 3.6μm photometry. We collected the IRAC 3.6μm photometry from the NASA/IPAC Extragalactic Database for the Roychowdhury et al. (2009) sample, and adopted a mass-to-light ratio corresponding to a Chabrier (2003) IMF following Leroy et al. (2008). Although the scatter is large, the observations are consistent with a dependence of the slope and zero point of the H I KS relation on stellar mass that is similar to what COLIBRE predicts. Because the predicted scatter is so large, much larger observational samples would be required to validate or refute our predictions.

4 REDSHIFT EVOLUTION OF THE KENNICUTT-SCHMIDT RELATION

4.1 The evolving KS relation from $z = 0$ to $z = 8$

Fig. 14 shows the evolution of the KS relation in HI, H_2 and total neutral hydrogen, from $z = 8$ to $z = 0$. COLIBRE predicts a monotonic evolution of the H_2 KS relation with time, so that the normalisation of the relation consistently decreases with time, maintaining a power-law index $N_{KS} \approx 1$ at all redshifts (at least at $\log_{10}(\Sigma_{H_2}/M_\odot\,pc^{-2}) \gtrsim 1$). The zero-point of the H_2 KS relation evolves very strongly with redshift, decreasing by a factor of ≈ 20 from $z = 8$ to $z = 0$.

The case of H I and total neutral hydrogen is more complex: at low gas surface densities $\lesssim 100\,M_\odot\,pc^{-2}$, the normalisation of the KS relation decreases mildly with increasing redshift from $z = 0$ to $z = 8$ (by ≈ 0.8 dex for H I and 0.4 dex for H I+H_2), while also becoming slightly steeper. This evolution reverses at a gas surface density $\approx 100\,M_\odot\,pc^{-2}$, resembling the evolution of the H_2 KS at higher surface densities.

Interestingly, we do not see a strong evolution in the scatter of the H_2 KS relation, which is inconsistent with the findings reported in other simulations, such as NewHorizon. Kraljic et al. (2024) find that the scatter in the H_2 KS relation in NewHorizon decreases by ≈ 0.25 dex from $z = 4$ to $z = 0.25$. There are several differences between our work and theirs; for example, they include all galaxies with stellar masses $\geq 10^7\,M_\odot$, while here we adopt a mass threshold that is 100 times higher. Another important difference is that NewHorizon does not directly model the formation of H_2, and hence it is assumed that thresholds in temperature and density are able to exclusively select H_2 gas. We demonstrated in Figs. 3 and 6 that this is not the case and, in fact, as the metallicity decreases, more of the cold gas can remain atomic. These differences make it hard to pinpoint the driver of the discrepancies but they certainly serve as a motivation to constrain these relations observationally. On the other hand, Shen et al. (2026) presented an analysis of the KS relation for total neutral gas at $z > 3$ for Thesan-zoom simulations measured at 1 kpc-scales. They found a steep relationship at high surface densities, $\Sigma_{HI+H_2} \gtrsim 10^{1.2}\,M_\odot\,pc^{-2}$, which agrees well with ours. At lower surface densities, their simulation predicts much higher Σ_{SFR} compared to COLIBRE, but this is a regime where Thesan-zoom is not well sampled given the small number of galaxies and the overall smaller number of low density regions with SFR > 0. The steep neutral KS relation is interpreted by Shen et al. (2026) as the result of turbulent energy balance in the ISM maintained by stellar feedback. The importance of turbulence in regulating star formation is also predicted by COLIBRE, as reported by Schaye et al. (2026).

The strong evolution of the zero point of the H_2 KS relation in COLIBRE is in part due to the evolution of the average gas metallicity of galaxies with $M_\star \geq 10^9\,M_\odot$. Fig. 15 shows the fraction of

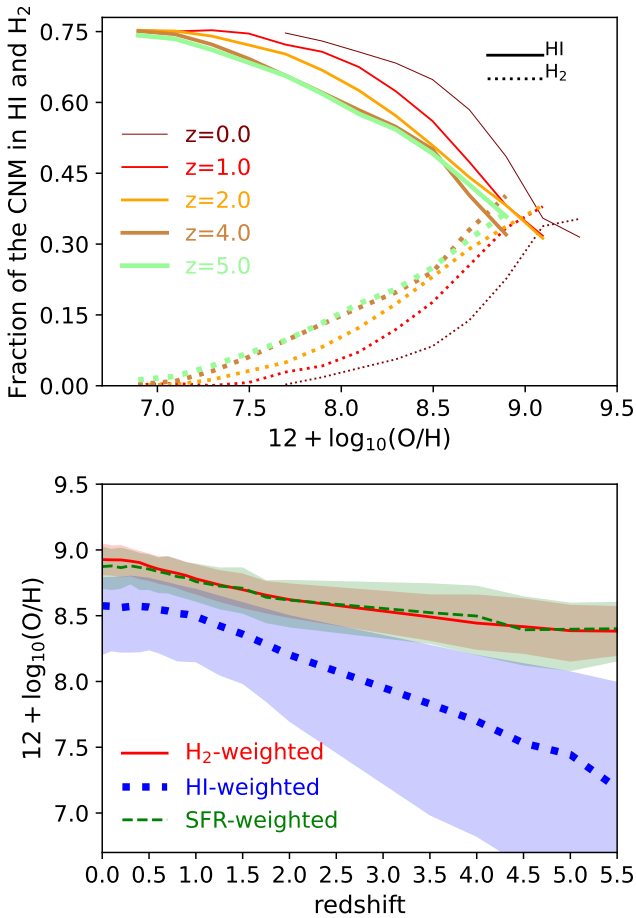

Figure 15. *Top panel:* The fraction of the CNM in H I (solid lines) and H_2 (dotted lines) as a function of gas metallicity, from $z = 0$ to $z = 5$ (see Eq. 2 for a definition of the CNM). We apply the same stellar and SFR selection of Fig. 6. Note that we only include a subset of the redshifts shown in Fig. 14 to avoid overlapping lines. *Bottom panel:* The redshift evolution of the median gas metallicity (solid lines), and the $25^{\rm th} - 75^{\rm th}$ percentile range (shaded regions), of galaxies with $M_\star \geq 10^9\,{\rm M}_\odot$, when weighted by the H_2 mass (solid line), H I mass (dotted line) or SFR (dashed line).

CNM in H I and H_2 as a function of the gas metallicity from $z = 0$ to $z = 5$ (similar to what Fig. 6 shows), and the evolution of the gas metallicity when weighted by different properties. First, we see that, at all redshifts, there is a clear trend of an increasing amount of the CNM being H I as the metallicity decreases. However, this relation is redshift dependent, with a decreasing fraction of the CNM in H I with increasing redshift at fixed gas metallicity. The corresponding simultaneously decreasing metallicity with redshift, leads to an overall effect of less H_2 and more H I being associated with a given amount of SFR with increasing redshift. This gives the impression that the molecular gas is more efficient at forming stars at high redshift, but this is primarily due to H_2 becoming a poorer tracer of star formation at high redshift, at least on kpc scales. We remind the reader that the star formation model in COLIBRE assumes a universal star formation efficiency per free fall time of 1% and a universal gravitational instability criterion to select star forming gas (Eq. 1), and hence there is no evolution built into the model. Thus, the strong evolution in the KS relation predicted by COLIBRE, particularly for H_2, is driven by the processes that govern the formation of H_2 and determine whether the gas is unstable and what the density distribution of the unstable gas is.

Fig. 15 shows that the gas metallicity weighted by the H I mass is always lower than the values weighted by SFR or H_2, with the differences becoming larger at higher redshifts. This is not surprising, as H I traces lower density gas than H_2 and SFR, which is typically located in the outskirts of galaxies, with most galaxies in COLIBRE having negative metallicity gradients (see Serrano Rodriguez et al. in preparation).

4.2 Comparison with observations of the resolved and global KS relation

In Fig. 16, we present comparisons with observations of the KS relation at $z > 0$. There are only very limited samples of galaxies at intermediate and high redshifts for which one can measure a resolved KS relation, and they correspond primarily to strongly lensed galaxies (e.g. Hodge et al. 2015; Sharon et al. 2013, 2019; Nagy et al. 2023). Note that at $z = 1$ the observations correspond to 6 galaxies (4 coming from Freundlich et al. 2013 and 2 from Nagy et al. 2023). At $z = 2$, there are observations for four galaxies, one is a submilimetre highly star-forming galaxy (Sharon et al. 2013); two are a pair of hyper-luminous IR galaxies (Gómez et al. 2025) separated by $\approx$ 85 kpc, one of which is mildly magnified; and a main-sequence galaxy (Sharon et al. 2019). At $z = 4$ the observations correspond to 5 galaxies (4 from Béthermin et al. 2023 and 1 from Hodge et al. 2015). In all cases, a constant (Milky-Way or starburst galaxy) CO-to-H_2 conversion factor was used. The conclusions we can draw from such a small sample are limited, but can serve as a reference to compare COLIBRE predictions with. We applied corrections to the SFR to convert them from a Salpeter or Kroupa IMF to a Chabrier IMF when necessary, and remove the helium contributions from the molecular gas if quantities reported include it.

At $z = 1$, we find that the global measurements of Nagy et al. (2023) agree well with the predicted relation for COLIBRE, but the individual regions (which sample a 800 pc scale) display a very large scatter, larger than the typical variations in COLIBRE. The resolved relations measured for the Cosmic snake and the sample of Freundlich et al. (2013) agree well with COLIBRE, but the individual regions in A521 tend to scatter down towards longer H_2 depletion times. At $z = 2$, we see that COLIBRE's median relation agrees better with the main sequence galaxy in Sharon et al. (2019), while the highly starbursting galaxies of Sharon et al. (2013); Gómez et al. (2025) lie (slightly) above the predicted relation. This shows that even within the small observational samples, there are hints that the normalisation of the KS relation varies with a galaxy's sSFR, in agreement with our predictions. At $z = 4$, we find that the observations sample Σ_{H_2} to values higher than what is typically reached by COLIBRE at m6 resolution, but the extrapolation of the predicted relation agrees well with what Hodge et al. (2015) report and is potentially above what Béthermin et al. (2023) measure. Larger samples are required to start to systematically probe the evolution of the resolved KS relation. This will become possible in the near future, for example with the extended Northern Extended Millimetre Array (NOEMA).

Unlike spatially resolved observations, integrated values for individual galaxies have been obtained by the thousands (Tacconi et al. 2020). From these observations, it has been well established that the H_2 depletion time decreases with increasing redshift. This is shown for COLIBRE and a compilation of observations in Fig. 17. The observations come from a range of H_2 tracers: CO, sub-millimetre or millimetre emission, or FIR SED. Even though they are all subject to different systematic effects, Tacconi et al. (2020) argue that they

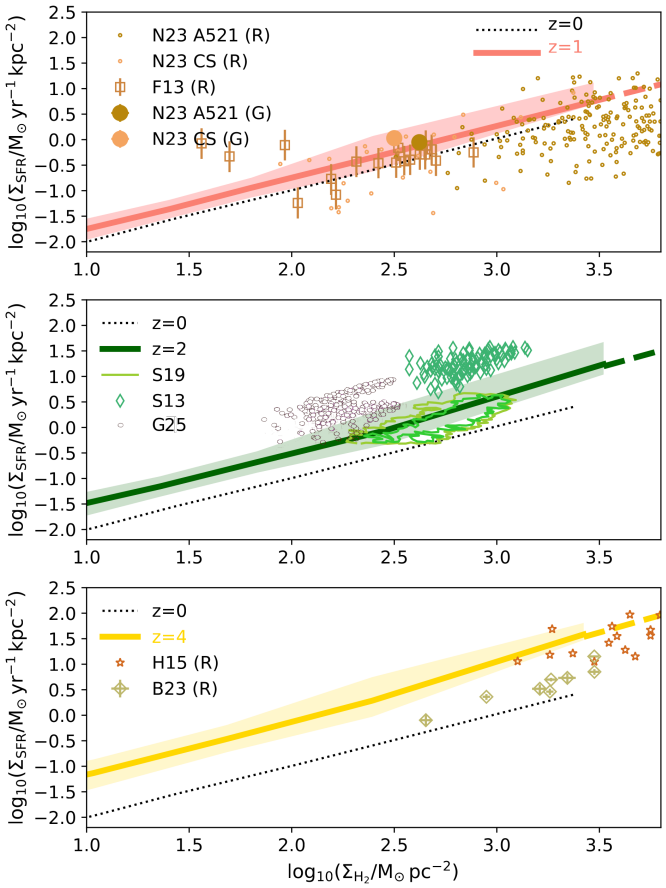

Figure 16. The predicted KS relation at $z = 1$ (top), $z = 2$ (middle) and $z = 4$ (bottom) for galaxies with $M_\star \geq 10^9\,M_\odot$. We compare with a compilation of observations of the (resolved) KS relation in individual galaxies. At $z = 1$, we show the resolved (R) and global (G) measurements of A521 and the Cosmic Snake from Nagy et al. (2023) (N+23). For the resolved data in N+23, we use the data provided in 800 pc apertures. We also show the resolved data from 4 massive star-forming galaxies at $z \approx 1.2$ from Freundlich et al. (2013). At $z = 2$ we compare with four galaxies; two from Sharon et al. (2013) (S13; a sub-millimetre galaxy at $z = 2.6$) and Sharon et al. (2019) (S19; a main sequence galaxy at $z = 2.26$); and a pair of two hyper-luminous IR galaxies from Gómez et al. (2025) (G25). For S13, we show the individual ≈ 2 kpc pixels; for S19 we show the contours tracing one and three pixels, where each pixel is of ≈ 2 kpc size (see Sharon et al. 2019 for details); while for G25 we show individual ≈ 2 kpc pixels for each galaxy. At $z = 4$, we show the results from 3 massive, star-forming galaxies from the ALPINE survey (Béthermin et al. 2023) (B23) at $z \approx 4.5$, and one submillitre galaxy at $z \approx 4$ Hodge et al. (2015) (H15). For COLIBRE, we show as dashed lines the extrapolation at high surface densities of the linear fit to the median relation (solid lines) measured at $1 \leq \log_{10}(\Sigma_{H_2}/M_\odot\,pc^{-2}) \leq 3$.

produce consistent H_2 scaling relations. Each circle represents an individual observed galaxy, while the stars show the median for the observations. The latter are computed with a minimum of 10 galaxies. We show with lines the predictions of COLIBRE, which are in remarkable agreement with the observations. However, we remind the reader that for COLIBRE we show individual 1 kpc rings rather than global measurements for galaxies, so the comparison is not one-to-one. Another important caveat is that we show regions from all galaxies with $M_\star \geq 10^9\,M_\odot$ and SFR > 0, while the observations

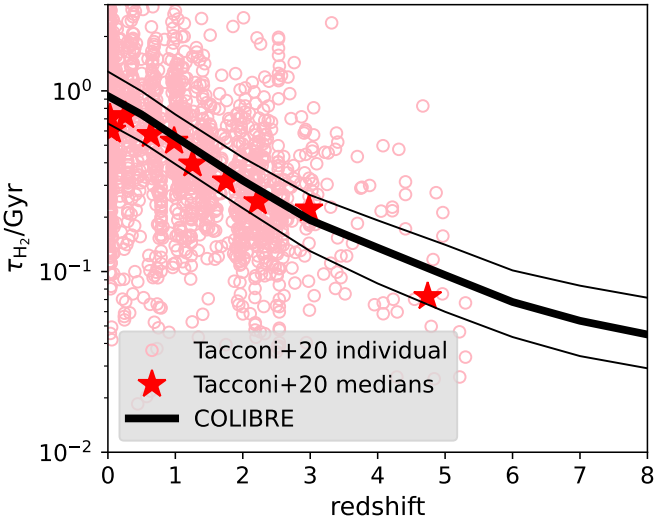

Figure 17. The evolution of the H_2 depletion time compared with the compilation of observations presented in Tacconi et al. (2020). Small circles correspond to individual galaxies, while the stars correspond to the medians computed from the observations. The thick and thin solid lines correspond to the median and $16^{th} - 84^{th}$ percentile ranges of all galaxies in COLIBRE with $M_\star \geq 10^9\,M_\odot$ and SFR > 0. To compute τ_{H_2}, we only considered 1 kpc annuli with $\Sigma_{H_2} > 1\,M_\odot\,pc^{-2}$, which correspond to the gas density regime where the L200m6 run is well converged (see Fig. A1) and comfortably includes the regimes from which observational results are computed.

are biased towards more massive galaxies with higher SFRs. Below we explore the effect of sSFR.

The scatter in the observations is large and driven by physical parameters, such as the sSFR of galaxies, which we show in Fig. 8 can systematically shift the H_2 depletion time. We demonstrate this at different redshifts in Fig. 18, where we plot the resolved H_2 depletion time as a function of a galaxy's sSFR in 5 redshift bins. At all redshifts, there is a strong dependence of the local τ_{H_2} on the global sSFR, with the zero point of the relation evolving strongly with redshift in COLIBRE. We also compute medians for the observations in redshift bins where there is enough data to have at least 10 points per bin. The observations agree strikingly well with our predictions, noting though that the observational samples are not stellar-mass complete, which our simulated sample is by construction. We also note that at the highest sSFR, the observations prefer slightly longer H_2 depletion times than what COLIBRE predicts at kpc scales. In the future we will compare global measurements to perform a fairer comparison with these global observations.

4.3 The evolving dependence of the scatter in the KS relation with local physical properties

Finally, in Fig. 19 we explore how some of the strongest correlations between τ_{H_2} and τ_{HI} with other local properties presented in Fig. 7 for $z = 0$ evolve with time. For τ_{H_2}, we find that the correlation with local gas metallicity remains strong with increasing redshift, with the amplitude of the correlation being close to redshift invariant. However, the correlation displays a saturation at the highest metallicities at any one redshift, with a reversal of the correlation at the high-metallicity end. We confirmed that the τ_{H_2}-gas metallicity correlation does not change when we increase the resolution, nor when we adopt instead the hybrid AGN feedback model (using the L025m5 and L050m6

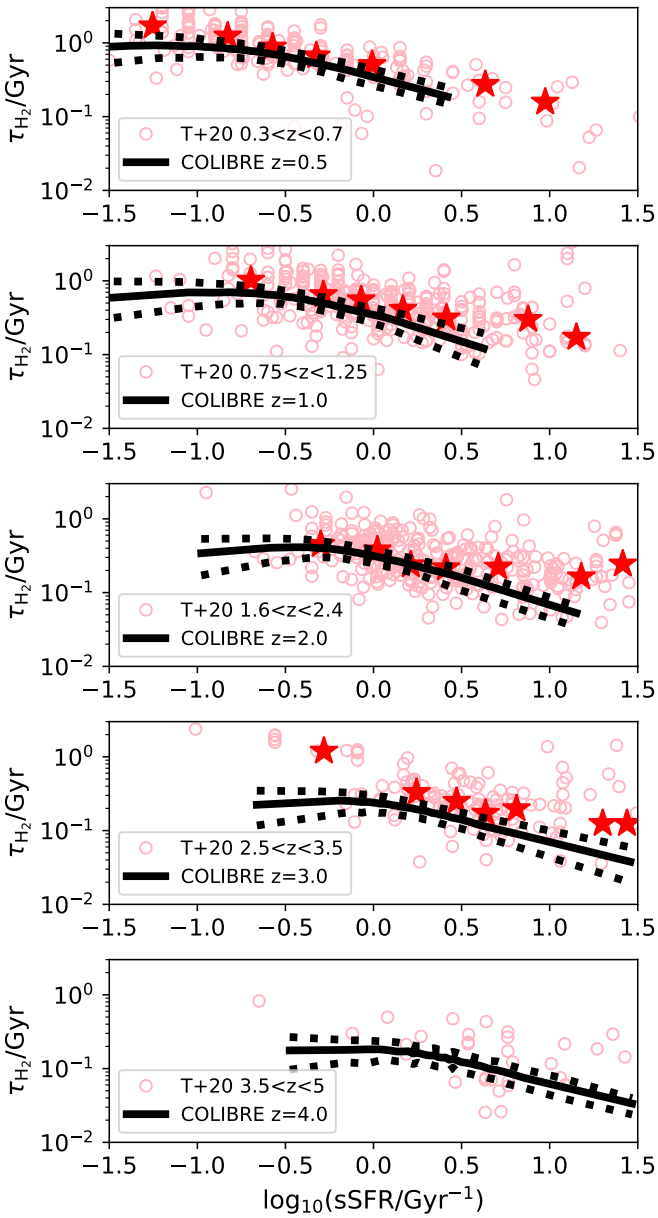

Figure 18. The H_2 depletion time as a function of sSFR for galaxies with $M_\star \geq 10^9\,M_\odot$, at different redshift bins from $z \approx 0.5$ to $z \approx 5$, compared with a compilation of observations presented in Tacconi et al. (2020). The solid and dashed lines in each panel show the median and $16^{th}-84^{th}$ percentile ranges, respectively, for galaxies in COLIBRE. Symbols are as in Fig. 17, and their corresponding redshift range are labelled in each panel. We do not show medians for the observations for the bottom panel due to the small number of galaxies.

Hybrid runs listed in Table 1). When using the L025m5 run, we find that the relation holds and the saturation manifests itself at the same τ_{H_2} values as in the L200m6 run. Interestingly, this saturation happens at $\approx 0.1/H(z)$, where $H(z)$ is Hubble's constant at redshift z. The latter corresponds to the free-fall time of a sphere of density $\sim 200\,\rho_{\rm crit}$, where $\rho_{\rm crit}$ is the critical density of the universe. Realistically, star formation cannot proceed any slower than that timescale, as $200\,\rho_{\rm crit}$ corresponds to the minimum gas density for gravitational collapse in a CDM universe. The redshift invariance of the τ_{H_2}-gas metallicity correlation implies that the physical mechanism behind it remains the same throughout cosmic time: as gas metallicity decreases, more of the star-forming gas is in the form of HI, and hence the amount of H_2 associated with a fixed SFR decreases. This was shown in Fig. 15.

The bottom-left panel of Fig. 19 shows that the correlation between τ_{H_2} and $s\Sigma_{\rm SFR}$ remains strong even up to $z = 8$, but with the normalisation of the relation decreasing strongly with redshift. This mirrors the strong evolution we see in the relation between τ_{H_2} and the global sSFR of galaxies in Fig. 18. Ignoring the saturation, the close to redshift invariance of the τ_{H_2}-metallicity relation suggests a more fundamental physical connection than that between τ_{H_2} and $s\Sigma_{\rm SFR}$, even if statistically the latter may be stronger in some regimes (as measured by the Spearman correlation coefficient).

In the top-right panel of Fig. 19, we show that the correlation between $\tau_{\rm HI}$ and metallicity evolves very strongly with redshift, with $\tau_{\rm HI}$ decreasing by two orders of magnitude from $z = 0$ to $z = 8$ at fixed local gas metallicity. The bottom-right panel of Fig. 19 shows that the relation between $\tau_{\rm HI}$ and $\Sigma_\star$ is already in place at $z = 8$ in COLIBRE, and evolves more mildly with redshift than the relation with local gas metallicity, with $\tau_{\rm HI}$ decreasing by a factor of ≈ 3 from $z = 0$ to $z = 8$ at fixed $\Sigma_\star$. For H I there is usually larger scatter in all the relations we explored compared with H_2, which is natural, as a significant fraction ($\gtrsim 50\%$) of the H I is not in the CNM, but instead in the WNM, which is less directly related to star formation.

Overall, our results show that the kpc-scale KS relation is already in place by $z = 8$ in COLIBRE. This is true for both the H I and H_2 KS relations. This contrasts with the predictions presented in Kraljic et al. (2024) for NewHorizon, in which they found that the KS relation is well established only at $z \lesssim 2-3$. However, as we mentioned above, there are important differences between our sample and theirs in terms of the stellar mass of galaxies covered, while also having several differences in the physical models. In the future, we want to investigate the impact on the KS relation of switching on and off various processes in COLIBRE, including, but not limited to, early stellar feedback, the non-equilibrium chemistry and the chemical diffusion model.

5 DISCUSSION AND CONCLUSIONS

We used the COLIBRE cosmological hydrodynamical simulations of galaxy formation to investigate the HI, H_2 and total neutral hydrogen Kennicutt-Schmidt (KS) relations and the scatter of these relations for galaxies with $M_\star \geq 10^9\,M_\odot$, over $0 \leq z \leq 8$. COLIBRE features on-the-fly non-equilibrium chemistry for H and He, with metals also included, in equilibrium but with non-equilibrium electron abundances, detailed radiative cooling down to ≈ 10 K, and live dust that impacts gas cooling and the formation of H_2. This detailed modelling enables direct predictions for the HI, H_2 and total neutral H KS relations.

We measure the KS relation using circular rings of fixed width in galaxies oriented face-on. We find, however, that modifying the method to measure the KS relation has only minimal effects on our results (Appendix A3). Our main findings are summarised below:

- COLIBRE accurately reproduces the observed HI, H_2, and total gas KS relations at $z = 0$ (Fig. 2), including their scatter, without having been explicitly tuned to these data. COLIBRE's star formation model assumes an underlying constant gas-to-star formation efficiency per free fall time of 1%, with the gas required to be gravitationally unstable at the resolution limit to form stars. This model, coupled with the sophisticated ISM model in COLIBRE, naturally

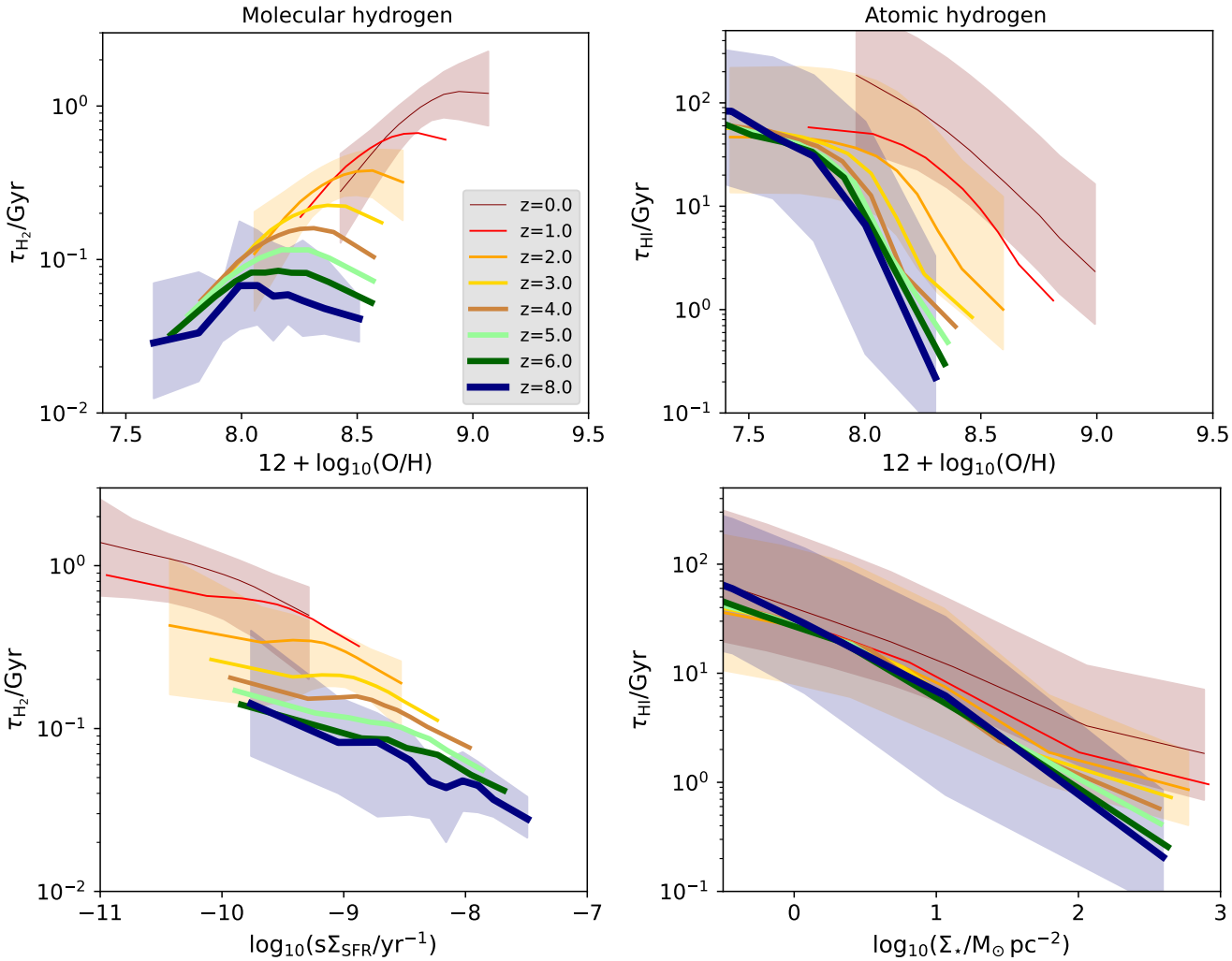

Figure 19. Evolution of some of the strongest resolved relations found in COLIBRE, between local galaxy properties and the kpc-scale H_2 (left) and H I (right) depletion timescales, for galaxies with $M_\star \geq 10^9\,M_\odot$. For H_2, we show the evolution of the relation between the resolved τ_{H_2} and the local gas metallicity (top-left panel) and sSFR surface density (bottom-left panel), between $z = 0$ and 8. Solid lines with shaded regions represent the medians with $16^{th} - 84^{th}$ percentile ranges (only shown for $z = 0$, 2 and 8), respectively, with the colours indicating different redshifts, as labelled in the top-left panel. For HI, we show the relation with local gas metallicity (top-right panel) and the stellar surface density (bottom-right panel).

captures differences in the KS relation amplitude and scatter between H I and H_2, with H I showing longer depletion times and larger scatter than H_2, consistent with the HI's association with more diffuse gas phases (Figs. 3, 4, and 6). The kpc-average KS relations are very well converged in COLIBRE, even when the numerical resolution is varied by 2 orders of magnitude.

- COLIBRE predicts the scatter in the KS relation to correlate strongly with local properties such as the stellar surface density, gas metallicity, and dust surface density (Figs. 5 and 7). At kpc scales, we find that lower metallicity/dust content regions form stars efficiently before significant H_2 formation, leading to apparently shorter H_2 and longer H I depletion times. The strongest predictors of H_2 depletion time are the local sSFR and gas metallicity, while H I depletion time correlates most strongly with the stellar surface density and dust content (Fig. 7).

- COLIBRE agrees remarkably well with spatially resolved observations at $z = 0$. In particular, we compared with ALMaQUEST, PHANGS and Wang et al. (2024) and found broad agreement in both the KS relation itself and its dependence on resolved properties such as sSFR and metallicity (Figs. 9, 10 and 11). COLIBRE also reproduces the lower KS amplitude in green-valley galaxies relative to main-sequence systems, matching ALMaQUEST and PHANGS (Fig. 12). We also explore KS fits performed on a galaxy-by-galaxy basis and find that COLIBRE predicts variations in the best fit parameters that resemble what observations indicate for H I and H_2 (Fig. 4), including a dependence of the best fit parameters on stellar mass for HI.

- While the global stellar mass plays a minor role in the normalisation of the KS relation (Fig. 8), the galaxy-wide sSFR has a stronger influence: high-sSFR galaxies have both larger cold gas reservoirs and higher star-formation efficiencies. We find that the enhanced efficiency is not purely due to gas content but also linked to higher conversion rates of gas into stars.

- The kpc-scale HI, H_2 and H I+H_2 KS relations are already in place by $z = 8$ in COLIBRE. At even higher redshifts, there are too few galaxies that meet our selection ($M_\star > 10^9\,M_\odot$ and SFR > 0) to clearly establish the presence of a KS relation. The H_2 depletion time decreases by a factor of ≈ 20 from $z = 0$ to $z = 8$ (Fig. 14), largely

driven by the lower local gas metallicities at higher redshift, leading to more HI-dominated cold neutral medium from which stars form (Fig. 15). The monotonic evolution of the H_2 KS relation contrasts with that of the HI, which shows a more complex evolution, with a transition at around $\Sigma_{\rm HI} \approx 100\,{\rm M}_\odot\,{\rm pc}^{-2}$. At lower gas surface densities, the amplitude of the H I KS relation decreases mildly with redshift, while at higher densities, the trend reverses.

- The overall lower gas metallicities at high redshifts predicted by COLIBRE lead to higher star formation efficiencies per unit H_2 in early galaxies, which is consistent with recent high-redshift constraints (Figs. 16, 17 and 18). The lower gas metallicity is associated with a cold neutral medium that is H I dominated, which once averaged on kpc scales, looks like having an efficient H_2 to SFR conversion. COLIBRE predicts a strong correlation between τ_{H_2} and sSFR, which agrees very well with observational constraints coming from integrated galaxy properties.

Our results demonstrate that the KS relation at kiloparsec scales for the H I and H_2 gas is an emergent outcome of the ISM physics (cooling, dust grains, metal enrichment, stellar feedback and non-equilibrium chemistry) and the underlying universal star formation efficiency included in the COLIBRE model. This is the case not only for the median KS relation, but also for the dependence of the scatter on local and global galaxy properties, and its very strong redshift evolution. The agreement with spatially resolved observations of the KS relations is a significant success of the COLIBRE model because none of the model's free parameters were adjusted to match these observations.

In the future we want to use variations of the COLIBRE physics, e.g. assuming chemical equilibrium, turning off the live dust model, varying the parameters of the star formation model and the stellar feedback, to isolate the physical mechanisms setting the amplitude and scatter of the KS relation at different cosmic epochs. This will also allow us to understand whether the KS relation can be used to study the interplay between galaxy-scale feedback effects and star formation.

One crucial limitation is the small observational samples of galaxies for which a resolved KS relation has been measured, and the ad-hoc galaxy selections. This complicates the testing of our predictions. Upcoming observations with ALMA of hundreds of local Universe galaxies[2] will allow the H_2 KS relation to be measured at kiloparsec scales for stellar-mass selected samples, and a robust characterisation of the scatter and its dependence on other local and global properties. Similarly, at higher redshifts, the combination of JWST and NOEMA/ALMA will allow increasing the sample of galaxies for which a resolved KS relation can be measured to dozens.

ACKNOWLEDGEMENTS

We thank Miroslava Dessauges, Anita Zanella, and Li-Hwai Lin for sharing their observational data in a format that facilitated the comparison with observations. We also acknowledge the PHANGS team for making the data presented in Sun et al. (2022) publicly available. CL also thanks the CONDOR and KILOGAS teams for useful discussions.

We acknowledge the use of SOAP (McGibbon et al. 2025) in our analysis, and thank their developers for the effort put in the code and documentation.

This work used the DiRAC@Durham facility managed by the Institute for Computational Cosmology on behalf of the STFC DiRAC HPC Facility (www.dirac.ac.uk). The equipment was funded by BEIS capital funding via STFC capital grants ST/K00042X/1, ST/P002293/1, ST/R002371/1 and ST/S002502/1, Durham University and STFC operations grant ST/R000832/1. DiRAC is part of the National e-Infrastructure. This work was also supported by resources provided by The Pawsey Supercomputing Centre with funding from the Australian Government and the Government of Western Australia. ABL acknowledges support by the Italian Ministry for Universities (MUR) program "Dipartimenti Di Eccellenza 2023-2027" within the Centro Bicocca di Cosmologia Quantitativa (BiCoQ), and support by UNIMIB's Fondo Di Ateneo Quota Competitiva (project 2024-ATEQC-0050). CSF acknowledges support from the European Research Council (ERC) Advanced Grant DMIDAS (GA 786910). FH acknowledges funding from the Netherlands Organization for Scientific Research (NWO) through research programme Athena 184.034.002. JT acknowledges support of a STFC Early Stage Research and Development grant (ST/X004651/1).

[2] https://www.kilogas.space/

DATA AVAILABILITY

The data supporting the plots within this article are available on reasonable request to the corresponding author. The COLIBRE simulation data will eventually be made publicly available, although we note that the data volume (several petabytes) may prevent us from simply placing the raw data on a server. In the meantime, people interested in using the simulations are encouraged to contact the corresponding author. A public version of the Swift code (Schaller et al. 2024) is available at http://www.swiftsim.com. The COLIBRE modules implemented in Swift will be made publicly available after the public release of the simulation data.

REFERENCES

Abbott T. M. C., Aguena M., Alarcon A., Allam S., Alves O., Amon A., Andrade-Oliveira F., Annis J. et al, 2022, Phys. Rev. D, 105, 023520
Agertz O., Kravtsov A. V., Leitner S. N., Gnedin N. Y., 2013, ApJ, 770, 25
Agertz O., Renaud F., Feltzing S., Read J. I., Ryde N., Andersson E. P., Rey M. P., Bensby T. et al, 2021, MNRAS, 503, 5826
Ali-Haïmoud Y., Bird S., 2013, MNRAS, 428, 3375
Aoyama S., Hou K.-C., Shimizu I., Hirashita H., Todoroki K., Choi J.-H., Nagamine K., 2017, MNRAS, 466, 105
Bahé Y. M., Schaye J., Schaller M., Bower R. G., Borrow J., Chaikin E., Kugel R., Nobels F. et al, 2022, MNRAS, 516, 167
Bellstedt S., Robotham A. S. G., 2024, arXiv:2410.17698, arXiv:2410.17698
Benítez-Llambay A., Ploeckinger S., Schaye J., Richings A. J., Chaikin E., Schaller M., Trayford J. W., Frenk C. S. et al, 2026, MNRAS, 546, stag268
Béthermin M., Accard C., Guillaume C., Dessauges-Zavadsky M., Ibar E., Cassata P., Devereaux T., Faisst A. et al, 2023, A&A, 680, L8
Bigiel F., Leroy A., Walter F., Blitz L., Brinks E., de Blok W. J. G., Madore B., 2010, AJ, 140, 1194
Bigiel F., Leroy A., Walter F., Brinks E., de Blok W. J. G., Madore B., Thornley M. D., 2008, AJ, 136, 2846
Bigiel F., Leroy A. K., Jiménez-Donaire M. J., Pety J., Usero A., Cormier D., Bolatto A., Garcia-Burillo S. et al, 2016, ApJ, 822, L26
Blitz L., Rosolowsky E., 2006, ApJ, 650, 933
Booth C. M., Schaye J., 2009, MNRAS, 398, 53
Borrow J., Schaller M., Bower R. G., Schaye J., 2022, MNRAS, 511, 2367
Chabrier G., 2003, PASP, 115, 763
Chaikin E., Schaye J., Schaller M., Benítez-Llambay A., Nobels F. S. J., Ploeckinger S., 2023, MNRAS, 523, 3709

Chaikin E., Schaye J., Schaller M., Ploeckinger S., Bahé Y. M., Benítez-Llambay A., Correa C., Forouhar Moreno V. J. et al, 2026, MNRAS, 548, stag300

Chandro-Gómez Á., Lagos C. d. P., Power C., Moreno V. J. F., Helly J. C., Lacey C. G., McGibbon R. J., Schaller M. et al, 2025, MNRAS, 539, 776

Correa C. A., Schaye J., Schaller M., Trayford J. W., Chaikin E., Benitez-Llambay A., Frenk C. S., Ploeckinger S. et al, 2026, MNRAS

Dalla Vecchia C., Schaye J., 2012, MNRAS, 426, 140

Davé R., Anglés-Alcázar D., Narayanan D., Li Q., Rafieferantsoa M. H., Appleby S., 2019, MNRAS, 486, 2827

Davé R., Crain R. A., Stevens A. R. H., Narayanan D., Saintonge A., Catinella B., Cortese L., 2020, MNRAS, 497, 146

Dehnen W., 2014, Computational Astrophysics and Cosmology, 1, 1

Dell'Agli F., García-Hernández D. A., Schneider R., Ventura P., La Franca F., Valiante R., Marini E., Di Criscienzo M., 2017, MNRAS, 467, 4431

Dey B., Rosolowsky E., Cao Y., Bolatto A., Sanchez S. F., Utomo D., Colombo D., Kalinova V. et al, 2019, MNRAS, 488, 1926

Diemer B., Sparre M., Abramson L. E., Torrey P., 2017, ApJ, 839, 26

Ellison S. L., Thorp M. D., Lin L., Pan H.-A., Bluck A. F. L., Scudder J. M., Teimoorinia H., Sánchez S. F. et al, 2020, MNRAS, 493, L39

Faucher-Giguère C.-A., 2020, MNRAS, 493, 1614

Federrath C., 2015, MNRAS, 450, 4035

Federrath C., Klessen R. S., 2012, ApJ, 761, 156

Feldmann R., Quataert E., Faucher-Giguère C.-A., Hopkins P. F., Çatmabacak O., Kereš D., Bassini L., Bernardini M. et al, 2023, MNRAS, 522, 3831

Forouhar Moreno V. J., Helly J., McGibbon R., Schaye J., Schaller M., Han J., Kugel R., 2025, arXiv e-prints, arXiv:2502.06932

Freundlich J., Combes F., Tacconi L. J., Cooper M. C., Genzel R., Neri R., Bolatto A., Bournaud F. et al, 2013, A&A, 553, A130

Gallagher M. J., Leroy A. K., Bigiel F., Cormier D., Jiménez-Donaire M. J., Ostriker E., Usero A., Bolatto A. D. et al, 2018, ApJ, 858, 90

Glover S. C. O., Clark P. C., 2012, MNRAS, 421, 9

Gómez J. S., Messias H., Nagar N. M., Orellana-González G., Ivison R. J., van der Werf P., 2025, A&A, 704, A178

Gonzalez-Perez V., Lacey C. G., Baugh C. M., Lagos C. D. P., Helly J., Campbell D. J. R., Mitchell P. D., 2014, MNRAS

Granato G. L., Ragone-Figueroa C., Taverna A., Silva L., Valentini M., Borgani S., Monaco P., Murante G. et al, 2021, MNRAS, 503, 511

Greif T. H., Glover S. C. O., Bromm V., Klessen R. S., 2009, MNRAS, 392, 1381

Han J., Cole S., Frenk C. S., Benitez-Llambay A., Helly J., 2018, MNRAS, 474, 604

Han J., Jing Y. P., Wang H., Wang W., 2012, MNRAS, 427, 2437

Hirashita H., Voshchinnikov N. V., 2014, MNRAS, 437, 1636

Hodge J. A., Riechers D., Decarli R., Walter F., Carilli C. L., Daddi E., Dannerbauer H., 2015, ApJ, 798, L18

Huško F., Lacey C. G., Schaye J., Schaller M., Chaikin E., Ploeckinger S., Benítez Llambay A., Richings A. J. et al, 2026, MNRAS, 547, stag324

Jiménez E., Lagos C. d. P., Ludlow A. D., Wisnioski E., 2023, MNRAS, 524, 4346

Jiménez-Donaire M. J., Bigiel F., Leroy A. K., Usero A., Cormier D., Puschnig J., Gallagher M., Kepley A. et al, 2019, ApJ, 880, 127

Jiménez-Donaire M. J., Brown T., Wilson C. D., Roberts I. D., Zabel N., Ellison S. L., Thorp M., Villanueva V. et al, 2023, A&A, 671, A3

Jönsson H., Allende Prieto C., Holtzman J. A., Feuillet D. K., Hawkins K., Cunha K., Mészáros S., Hasselquist S. et al, 2018, AJ, 156, 126

Kennicutt Jr. R. C., 1983, ApJ, 272, 54

—, 1989, ApJ, 344, 685

Kobayashi C., Umeda H., Nomoto K., Tominaga N., Ohkubo T., 2006, ApJ, 653, 1145

Kraljic K., Renaud F., Dubois Y., Pichon C., Agertz O., Andersson E., Devriendt J., Freundlich J. et al, 2024, A&A, 682, A50

Kroupa P., 2001, MNRAS, 322, 231

Krumholz M. R., McKee C. F., 2005, ApJ, 630, 250

Lacey C. G., Baugh C. M., Frenk C. S., Benson A. J., Bower R. G., Cole S., Gonzalez-Perez V., Helly J. C. et al, 2016, MNRAS, 462, 3854

Lagos C. d. P., Bravo M., Tobar R., Obreschkow D., Power C., Robotham A. S. G., Proctor K. L., Hansen S. et al, 2024, MNRAS, 531, 3551

Lagos C. d. P., Crain R. A., Schaye J., Furlong M., Frenk C. S., Bower R. G., Schaller M., Theuns T. et al, 2015, MNRAS, 452, 3815

Lagos C. D. P., Lacey C. G., Baugh C. M., Bower R. G., Benson A. J., 2011, MNRAS, 416, 1566

Lagos C. d. P., Schaye J., Bahé Y., Van de Sande J., Kay S. T., Barnes D., Davis T. A., Dalla Vecchia C., 2018, MNRAS, 476, 4327

Lee J. C., Gil de Paz A., Tremonti C., Kennicutt Jr. R. C., Salim S., Bothwell M., Calzetti D., Dalcanton J. et al, 2009, ApJ, 706, 599

Leroy A. K., Walter F., Brinks E., Bigiel F., de Blok W. J. G., Madore B., Thornley M. D., 2008, AJ, 136, 2782

Leroy A. K., Walter F., Sandstrom K., Schruba A., Munoz-Mateos J.-C., Bigiel F., Bolatto A., Brinks E. et al, 2013, AJ, 146, 19

Leung S.-C., Nomoto K., 2019, Publ. Astron. Soc. Australia, 36, e006

Lin L., Ellison S. L., Pan H.-A., Thorp M. D., Yu P.-C., Belfiore F., Hsieh B.-C., Maiolino R. et al, 2022, ApJ, 926, 175

Lin L., Pan H.-A., Ellison S. L., Belfiore F., Shi Y., Sánchez S. F., Hsieh B.-C., Rowlands K. et al, 2019, ApJ, 884, L33

Ludlow A. D., Fall S. M., Schaye J., Obreschkow D., 2021, MNRAS, 508, 5114

Ludlow A. D., Fall S. M., Wilkinson M. J., Schaye J., Obreschkow D., 2023, MNRAS, 525, 5614

Ludlow A. D., Schaye J., Schaller M., Richings J., 2019, MNRAS, 488, L123

Martínez-Serrano F. J., Serna A., Domínguez-Tenreiro R., Mollá M., 2008, MNRAS, 388, 39

McClure-Griffiths N. M., Stanimirović S., Rybarczyk D. R., 2023, ARA&A, 61, 19

McGibbon R., Helly J., Schaye J., Schaller M., Vandenbroucke B., 2025, The Journal of Open Source Software, 10, 8252

Nagy D., Dessauges-Zavadsky M., Messa M., Richard J., Sun J., Combes F., Eyholzer Y., 2023, A&A, 678, A183

Nobels F. S. J., Schaye J., Schaller M., Ploeckinger S., Chaikin E., Richings A. J., 2024, MNRAS, 532, 3299

Nomoto K., Kobayashi C., Tominaga N., 2013, ARA&A, 51, 457

Nomoto K., Tominaga N., Umeda H., Kobayashi C., Maeda K., 2006, Nuclear Phys. A, 777, 424

Orr M. E., Hayward C. C., Hopkins P. F., Chan T. K., Faucher-Giguère C.-A., Feldmann R., Kereš D., Murray N. et al, 2018, MNRAS, 478, 3653

Ostriker E. C., McKee C. F., Leroy A. K., 2010, ApJ, 721, 975

Park H.-J., Battisti A. J., Marchal A., Cortese L., Wisnioski E., Seibert M., Kim S.-J., McClure-Griffiths N. et al, 2025, MNRAS, 540, 2623

Pessa I., Schinnerer E., Belfiore F., Emsellem E., Leroy A. K., Schruba A., Kruijssen J. M. D., Pan H. A. et al, 2021, A&A, 650, A134

Pillepich A., Springel V., Nelson D., Genel S., Naiman J., Pakmor R., Hernquist L., Torrey P. et al, 2018, MNRAS, 473, 4077

Ploeckinger S., Richings A. J., Schaye J., Trayford J. W., Schaller M., Chaikin E., 2025, arXiv e-prints, arXiv:2506.15773

Ploeckinger S., Schaye J., 2020, MNRAS, 497, 4857

Portinari L., Chiosi C., Bressan A., 1998, A&A, 334, 505

Richings A. J., Faucher-Giguère C.-A., Gurvich A. B., Schaye J., Hayward C. C., 2022, MNRAS, 517, 1557

Richings A. J., Schaye J., Oppenheimer B. D., 2014a, MNRAS, 440, 3349

—, 2014b, MNRAS, 442, 2780

Roychowdhury S., Chengalur J. N., Begum A., Karachentsev I. D., 2009, MNRAS, 397, 1435

Salpeter E. E., 1955, ApJ, 121, 161

Schaller M., Borrow J., Draper P. W., Ivkovic M., McAlpine S., Vandenbroucke B., Bahé Y., Chaikin E. et al, 2024, MNRAS, 530, 2378

Schaye J., 2001, ApJ, 562, L95

—, 2004, ApJ, 609, 667

Schaye J., Chaikin E., Schaller M., Ploeckinger S., Huško F., McGibbon R. J., Trayford J. W., Benítez-Llambay A. et al, 2026, MNRAS, 548, stag375

Schaye J., Crain R. A., Bower R. G., Furlong M., Schaller M., Theuns T., Dalla Vecchia C., Frenk C. S. et al, 2015, MNRAS, 446, 521

Schinnerer E., Leroy A. K., 2024, ARA&A, 62, 369

Schmidt M., 1959, ApJ, 129, 243

Schruba A., Leroy A. K., Walter F., Bigiel F., Brinks E., de Blok W. J. G., Dumas G., Kramer C. et al, 2011, AJ, 142, 37

Segovia Otero Á., Agertz O., Renaud F., Kraljic K., Romeo A. B., Semenov V. A., 2025, MNRAS, 538, 2646
Semenov V. A., Kravtsov A. V., Gnedin N. Y., 2018, ApJ, 861, 4
Sharon C. E., Baker A. J., Harris A. I., Thomson A. P., 2013, ApJ, 765, 6
Sharon C. E., Tagore A. S., Baker A. J., Rivera J., Keeton C. R., Lutz D., Genzel R., Wilner D. J. et al, 2019, ApJ, 879, 52
Shen S., Wadsley J., Stinson G., 2010, MNRAS, 407, 1581
Shen X., Kannan R., Puchwein E., Smith A., Vogelsberger M., Borrow J., Garaldi E., Keating L. et al, 2026, MNRAS, 545, staf2119
Shi Y., Helou G., Yan L., Armus L., Wu Y., Papovich C., Stierwalt S., 2011, ApJ, 733, 87
Shi Y., Yan L., Armus L., Gu Q., Helou G., Qiu K., Gwyn S., Stierwalt S. et al, 2018, ApJ, 853, 149
Somerville R. S., Popping G., Trager S. C., 2015, MNRAS, 453, 4337
Sun J., Leroy A. K., Rosolowsky E., Hughes A., Schinnerer E., Schruba A., Koch E. W., Blanc G. A. et al, 2022, AJ, 164, 43
Tacconi L. J., Genzel R., Sternberg A., 2020, ARA&A, 58, 157
Trayford J. W., Schaye J., Correa C., Ploeckinger S., Richings A. J., Chaikin E., Schaller M., Benitez-Llambay A. et al, 2025, arXiv e-prints, arXiv:2505.13056
Tremmel M., Karcher M., Governato F., Volonteri M., Quinn T. R., Pontzen A., Anderson L., Bellovary J., 2017, MNRAS, 470, 1121
Tremonti C. A., Heckman T. M., Kauffmann G., Brinchmann J., Charlot S., White S. D. M., Seibert M., Peng E. W. et al, 2004, ApJ, 613, 898
Tsai J. C., Mathews W. G., 1995, ApJ, 448, 84
Usero A., Leroy A. K., Walter F., Schruba A., García-Burillo S., Sandstrom K., Bigiel F., Brinks E. et al, 2015, AJ, 150, 115
Walter F., Brinks E., de Blok W. J. G., Bigiel F., Kennicutt R. C., Thornley M. D., Leroy A., 2008, AJ, 136, 2563
Wang J., Lin X., Staveley-Smith L., Yang D., Walter F., Liang Z., Shi Y., Fu J. et al, 2024, ApJ, 973, 15
Wiersma R. P. C., Schaye J., Theuns T., Dalla Vecchia C., Tornatore L., 2009, MNRAS, 399, 574
Wong T., Cao Y., Luo Y., Bolatto A. D., Sánchez S. F., Barrera-Ballesteros J. K., Blitz L., Colombo D. et al, 2024, ApJS, 271, 35
Xie L., De Lucia G., Hirschmann M., Fontanot F., Zoldan A., 2017, MNRAS, 469, 968
Zanella A., Iani E., Dessauges-Zavadsky M., Richard J., De Breuck C., Vernet J., Kohandel M., Arrigoni Battaia F. et al, 2024, A&A, 685, A80
Zhukovska S., Gail H. P., Trieloff M., 2008, A&A, 479, 453

APPENDIX A: CONVERGENCE OF THE KS RELATION

A1 Convergence with the resolution of the simulation

The top and middle panels of Fig. A1 show the KS relations for the atomic, molecular and total neutral hydrogen at $z = 0$ and 2 for the three L025 simulations listed in Table 1.

For HI, we see that the convergence at $z = 0$ is excellent, with differences between resolutions only apparent in the scatter of the relation. The resolution m5 produces the largest scatter (by 0.15 dex), consistent with Fig. 13. At $z = 2$, there are differences between the three resolutions at low surface densities of HI, $\log_{10}(\Sigma_{\rm HI}/{\rm M}_\odot\,{\rm pc}^{-2}) \lesssim 1$. Below that surface density, m5 displays the steepest relationship (at $0 \lesssim \log_{10}(\Sigma_{\rm HI}/{\rm M}_\odot\,{\rm pc}^{-2}) \lesssim 1$). In that regime, it follows the same slope as predicted for higher surface densities.

For H_2, we see good convergence at high surface densities. At m5 resolution, the KS slope of ≈ 1 is present at all densities $\gtrsim 0.1\,{\rm M}_\odot\,{\rm pc}^{-2}$. For m6 resolution, we start to see a flattening of the KS relation and a deviation from m5 resolution below $\approx 1\,{\rm M}_\odot\,{\rm pc}^{-2}$. For m7 resolution, this deviation occurs at higher densities, $\approx 10\,{\rm M}_\odot\,{\rm pc}^{-2}$. At $z = 2$, the deviations from the m5 resolution results move to lower H_2 surface densities, so that convergence is achieved already at $\gtrsim 0.1\,{\rm M}_\odot\,{\rm pc}^{-2}$. Nobels et al. (2024) used idealised galaxy disks to show that the molecular KS relation did not converge at low gas surface densities, which agrees with what we find in the fully cosmological set-up of COLIBRE.

For the total H I+H_2 KS relation, we see very similar behaviour to that obtained for the H I KS relation.

For our fiducial m6 resolution, this means that our results are converged at the typical surface densities probed by observations, $\gtrsim 10\,{\rm M}_\odot\,{\rm pc}^{-2}$ for H_2 and $\gtrsim 1{\rm M}_\odot\,{\rm pc}^{-2}$ for HI.

Fig. A2 shows the differences in the KS relation normalisation between m6 and m5 for galaxies at $z = 0$ selected in bins of stellar mass. We find that galaxies at m6 resolution with stellar masses $10^8 - 10^9\,{\rm M}_\odot$ can show deviations of up to 0.6 dex in the normalisation of the total KS relation (right panel) relative to the m5 run. We thus decide to impose a minimum stellar mass of $10^9\,{\rm M}_\odot$ for our analysis of the L200m6 run, but noting that there is no clear stellar mass threshold above which the KS relation is fully converged. This will depend on how star-forming/gas-rich a galaxy is, and which gas surface densities we sample. Nevertheless, we consider the stellar mass threshold above to be a reasonable compromise between probing a large dynamic range while also avoiding galaxies that are more affected by resolution.

The analysis above is for the predicted average KS relation. The convergence of the scaling relations between the molecular and atomic depletion times and the several local galaxy properties analysed in § 3.2.1 is not guaranteed and needs to be explicitly tested. Fig. A3 shows the dependence of the H_2 and H I gas depletion times and the 5 properties shown in Fig. 7. In the case of $\tau_{\rm HI}$, Fig. A3 shows an overall good convergence between the three resolutions. This agrees with the convergence seen in the average H I KS relation in Fig. A1. The convergence is particularly good for the properties that are most strongly correlated with $\tau_{\rm HI}$, i.e. $\Sigma_\star$ and $\Sigma_{\rm dust}$.

For τ_{H_2} we see that the m5 and m6 resolutions produce very similar correlations with the dust surface density, local sSFR, cool gas velocity dispersion and stellar surface density. The m7 resolution clearly deviates from the relations obtained at higher resolutions. The gas metallicity (top-left panel) shows that the m5 and m6 resolution exhibit significant differences, particularly in low metallicity gas ($12 + \log_{10}({\rm O/H}) \lesssim 8.7$). This may not be surprising given the different densities at which stars form in the m5 and m6 resolutions at low gas metallicity (Fig. 6). Schaye et al. (2026) shows that the stellar mass-gas metallicity relation predicted by COLIBRE at $z = 0$ does not converge well between the runs at m5 and m6 resolution for low-mass, low-gas metallicity galaxies ($M_\star \lesssim 10^{9.3}\,{\rm M}_\odot$).

Despite some differences found between resolutions, the strengths of the correlations shown in Fig. 7 converge quite well. We show this in Table A1. The strongest correlations in terms of Spearman's correlation coefficient R are the same for the three resolutions. The

Table A1. The Spearman correlation coefficient, R, for the correlation between $\log_{10}(\tau_{H_2})$ or $\log_{10}(\tau_{\rm HI})$ and 5 local properties listed in each row. This is shown for the L025m5, L025m6 and L025m7 simulations for galaxies with $M_\star > 10^9\,{\rm M}_\odot$ and SFR > 0 at $z = 0$. Units used for each property are as in Fig. A3. Fig. 7 shows these values for the L200m6 run we use throughout the paper.

	$\log_{10}(\tau_{\rm HI})$	$\log_{10}(\tau_{H_2})$
$\log_{10}(\Sigma_\star)$	-0.66, -0.68, -0.74	0.32, 0.42, 0.35
$\log_{10}(s\Sigma_{\rm SFR})$	-0.35, -0.34, -0.27	-0.52, -0.56, -0.44
$12 + \log_{10}({\rm O/H})$	-0.27, -0.35, -0.38	0.24, 0.32, 0.36
$\log_{10}(\Sigma_{\rm dust})$	-0.62, -0.71, -0.77	0.26, 0.36, 0.32
$\log_{10}(\sigma_{\rm cool})$	0.09, 0.14, 0.14	-0.08, -0.10, -0.03

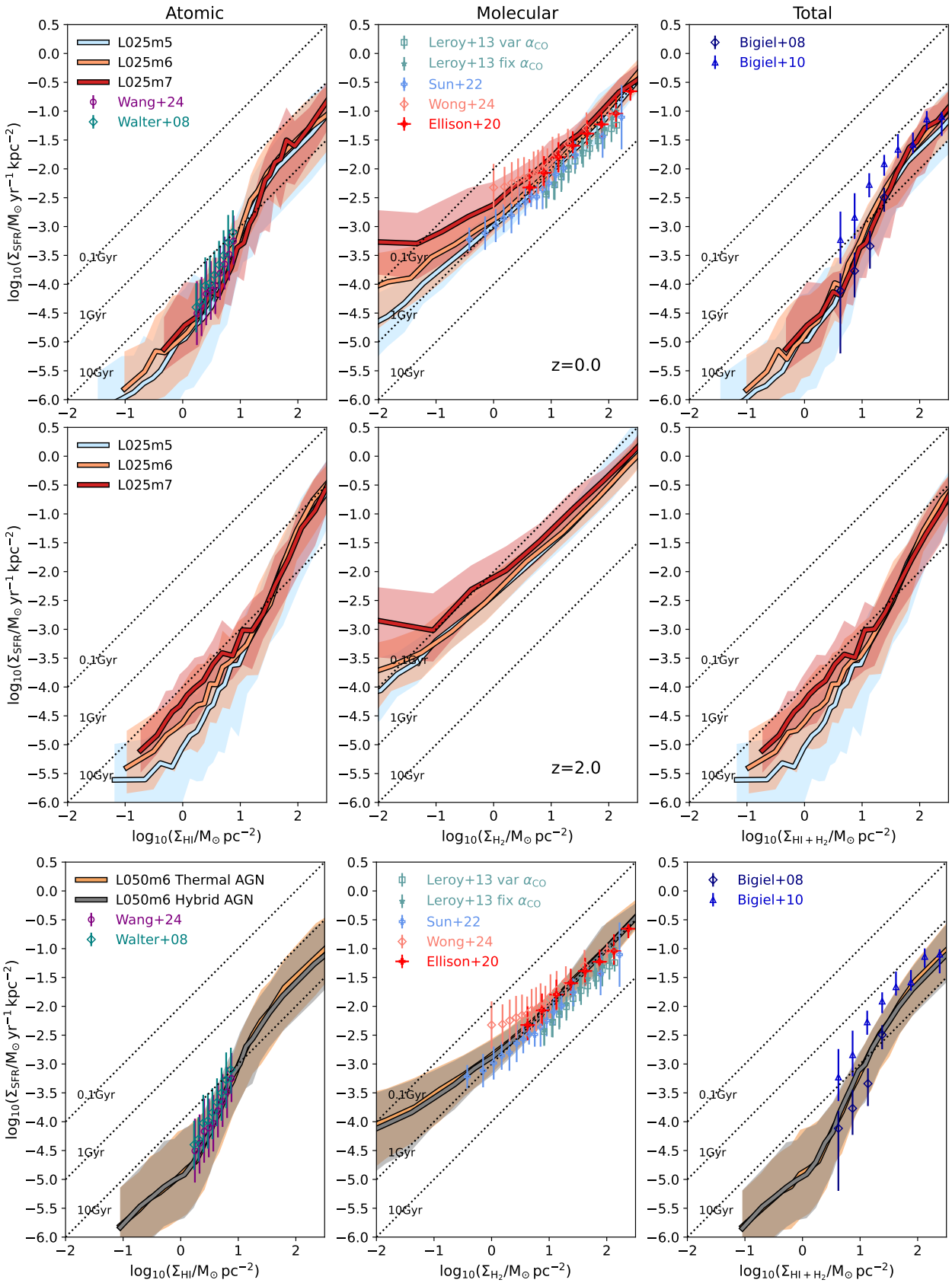

Figure A1. As Fig. 2 but for the simulations L025m5, L025m6 and L025m7, as labelled, at $z = 0$ (top) and $z = 2$ (middle). The bottom panel shows the $z = 0$ KS relation again, but for the runs L050m6 Thermal and Hybrid, as labelled. Table 1 summarises the runs used in this figure. Observations are only shown in the top and bottom panels.

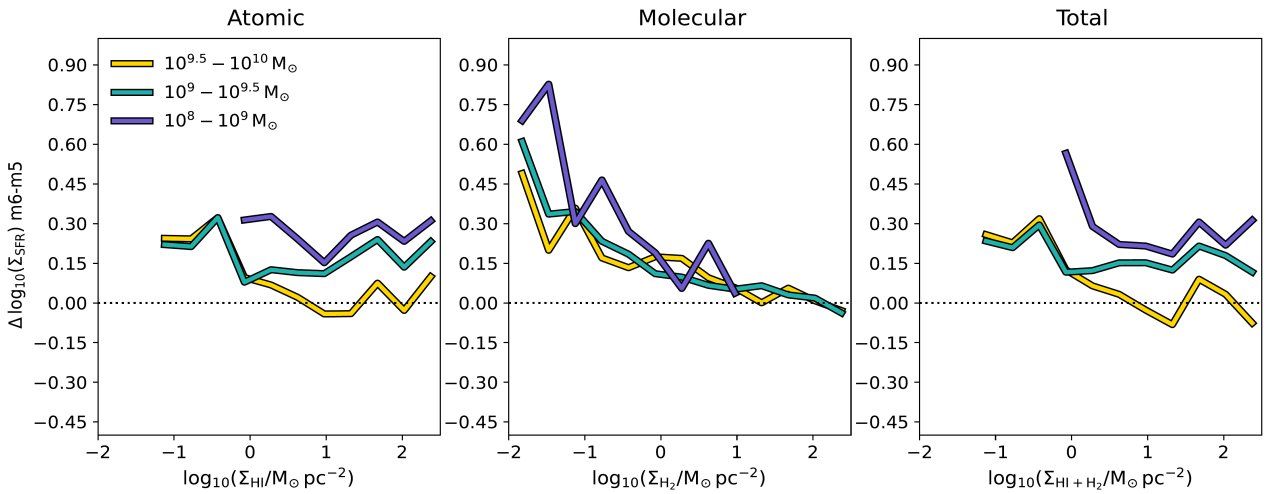

Figure A2. The difference between $\log_{10}(\Sigma_{\rm SFR})$ in the L025m5 and L025m6 runs in bins of $\log_{10}(\Sigma_{\rm gas})$, for galaxies at $z = 0$ selected in different ranges stellar mass, as labelled in the left panel. The differences become smaller as we move towards more massive galaxies. In the right panel, the lowest mass galaxies in the L025m6 display differences in $\log_{10}(\Sigma_{\rm SFR})$ of up to 0.6 dex compared to L025m5.

general trend is that the m5 resolution tends to display a larger scatter in the correlations between $\tau_{\rm HI}$ or $\tau_{\rm H_2}$ and the five properties listed in Table A1, leading to slightly lower values of R.

A2 Convergence with the adopted AGN feedback model

The bottom panels of Fig. A1 show the KS relations predicted by the L050m6 Thermal and Hybrid AGN feedback runs (listed in Table 1). This is shown at $z = 0$ and for the same stellar mass and SFR selection. The predicted relations are very similar including the medians and scatter. The figure confirms that the adopted AGN feedback model has a negligible impact on the predicted KS relation in COLIBRE, and justifies our decision to carry out most of the analysis using runs with thermal AGN feedback only.

A3 Convergence between the methods used to measure the KS relation

Besides the method "Annuli on face-on galaxy", we also implemented other methods to measure maps of the SFR and gas surface densities with the purpose of studying how well the resulting KS converges between these different methods.

Below, we summarise the methods explored:

- *Annuli on randomly-oriented galaxy:* This method starts by taking the simulation box XY projection, and then following the same procedure as described for the ANNULI-FACE method described in § 2.2. We refer to this method as ANNULI-RAND.
- *Regular grid on face-on galaxy:* This method also starts from the galaxies oriented face-on, which is computed as described for the ANNULI-FACE method. Then, all particles within a square of 50 pkpc are selected. We then grid the space using regular square pixels of size $\Delta r \times \Delta r$. We compute for each pixel the masses, SFRs and metallicities following the ANNULI-FACE method but using only the particles that fall in the pixel. We refer to this method as GRID-FACE. Surface densities are then computed using the area of the pixel.
- *Regular grid on randomly-oriented galaxy:* This method follows the description provided for GRID-FACE, but the grid is constructed over the galaxy projected onto the simulation box XY's coordinates, as is done for ANNULI-RAND. We refer to this method as GRID-RAND.

We remind the reader that our fiducial method bins galaxies in circular apertures of $\Delta r = 1$ kpc after orienting them face-on, and with a fiducial minimum number of particles per bin of $N_{\rm min} = 10$.

In the following, we compare different methods of measuring the KS relation at $z = 0$ in the L025m6 run to determine whether our results are robust against the choices we make about how to measure the KS relation.

The top panels of Fig. A4 shows a comparison of the 4 different methods used in this paper to measure the KS relation. For H_2 (top-middle), we find excellent agreement between methods at $\log_{10}(\Sigma_{\rm H_2}/{\rm M_\odot\,pc^{-2}}) \gtrsim 0.5 - 1.8$, which is the regime in which observations are available. At lower and higher surface densities, we start to see some differences in the median, but they are still well within the scatter of the correlation.

For H I (top-left panel in Fig. A4), we see more systematic differences between methods, with the ones adopting a random orientation leading to a slightly higher normalisation than those adopting a face-on orientation. This is naturally expected in situations where the H I disk has a larger scaleheight than the disk traced by the instantaneous SFR. The latter is expected in COLIBRE given the hotter nature of H I compared to the gas particles with SFR > 0 (see Fig. 3). Regardless, the differences in normalisation are within ≈ 0.2 dex, well below the intrinsic scatter of the H I KS relation in COLIBRE.

For the total H I+H_2 (top-right panel of Fig. A4), the systematic differences between methods are smaller than those seen for HI, but go in the same direction, with the methods using face-on orientation producing a slightly lower normalisation of the KS relation than those using random orientations.

The middle and lower panels of Fig. A4 show the KS relations obtained for COLIBRE using the ANNULI-FACE method, but varying Δr (the width of the circular bins) and $N_{\rm min}$ (the minimum number of particles required per circular bin), as labelled. In both cases we see excellent convergence in the shape and scatter of the KS relation in all neutral hydrogen phases. The main difference we see is that increasing $N_{\rm min}$ leads to a poorer sampling of the low surface density regime, but without introducing a significant bias.

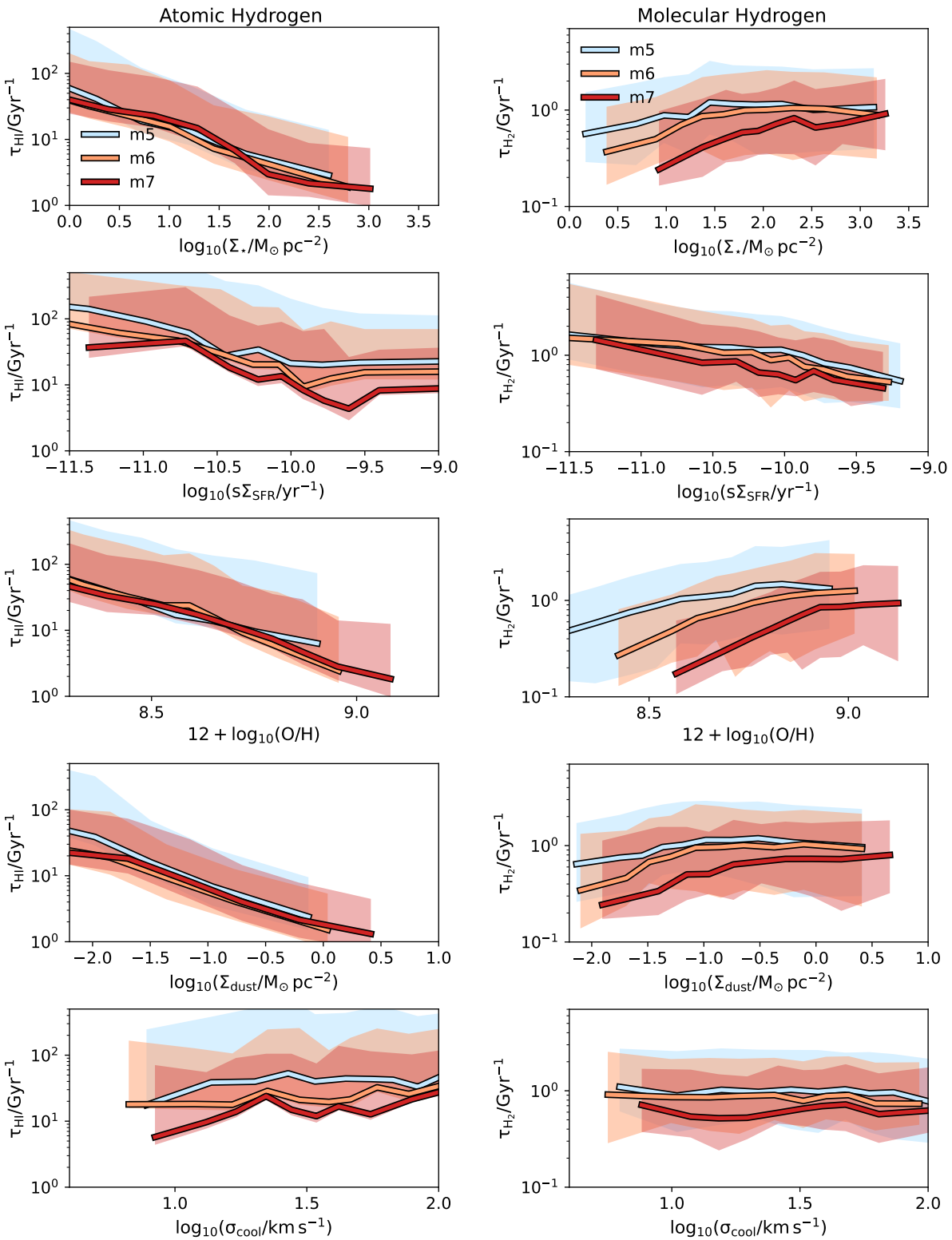

Figure A3. The relation between the depletion times of H I (left) and H_2 (right) and the 5 local properties analysed in Fig. 7-from top to bottom stellar surface density, local sSFR, gas metallicity, dust surface density, and cool gas velocity dispersion. This is shown for the L025m5, L025m6 and L025m7 as labelled in the top panels. In the three runs we include galaxies with $M_\star > 10^9\,M_\odot$ and SFR > 0 at $z = 0$.

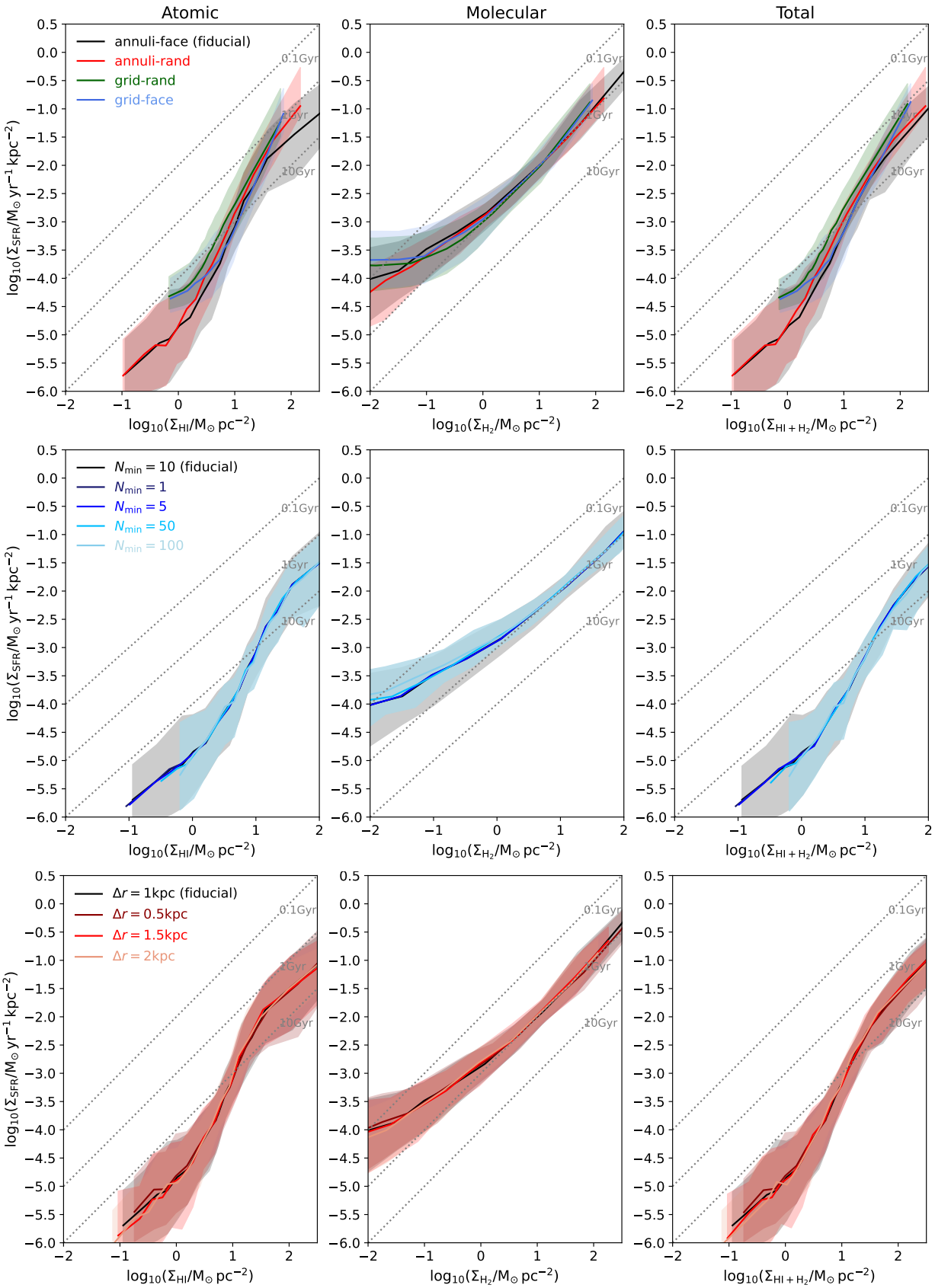

Figure A4. The HI, H_2 and H I+H_2 KS relations, as labelled at the top, at $z = 0$ in the L025m6 run of Table 1, measured using different methods (top); using our fiducial ANNULI-FACE method but adopting different thresholds for the minimum number of gas particles in a annulus (middle); and adopting different widths for the annuli (bottom). In all panels lines show medians, while the shaded regions indicate the $16 - 84^{\rm th}$ percentile ranges. Not not overwhelm the figure, in the middle panel we only show the $16 - 84^{\rm th}$ percentile ranges for $N_{\rm min} = 10$ and $= 100$, while for the other panels we show medians and percentile ranges for all the samples. We find excellent convergence in the predicted KS relation against methods and the specific choices of each method.

Overall, Fig. A4 demonstrate that the predicted KS relation in COLIBRE at the m6 resolution is robust against variants in the methods used to measure it.

APPENDIX B: ADDITIONAL VISUALISATION EXAMPLES

Fig. B1 shows examples of star-forming galaxies (top) and passive galaxies (bottom) at $z = 0$ in the L025m6 run. The stellar mass and its hierarchy (whether it is a central or a satellite galaxy) are shown in the top panels. In general and at this resolution, we see that star-forming galaxies sample H_2 surface densities in excess of $\log_{10}(\Sigma_{H_2}/M_\odot\,pc^{-2}) \gtrsim 1.5$, while galaxies below the main sequence rarely have H_2 gas that reaches such high densities.

This paper has been typeset from a TEX/LATEX file prepared by the author.

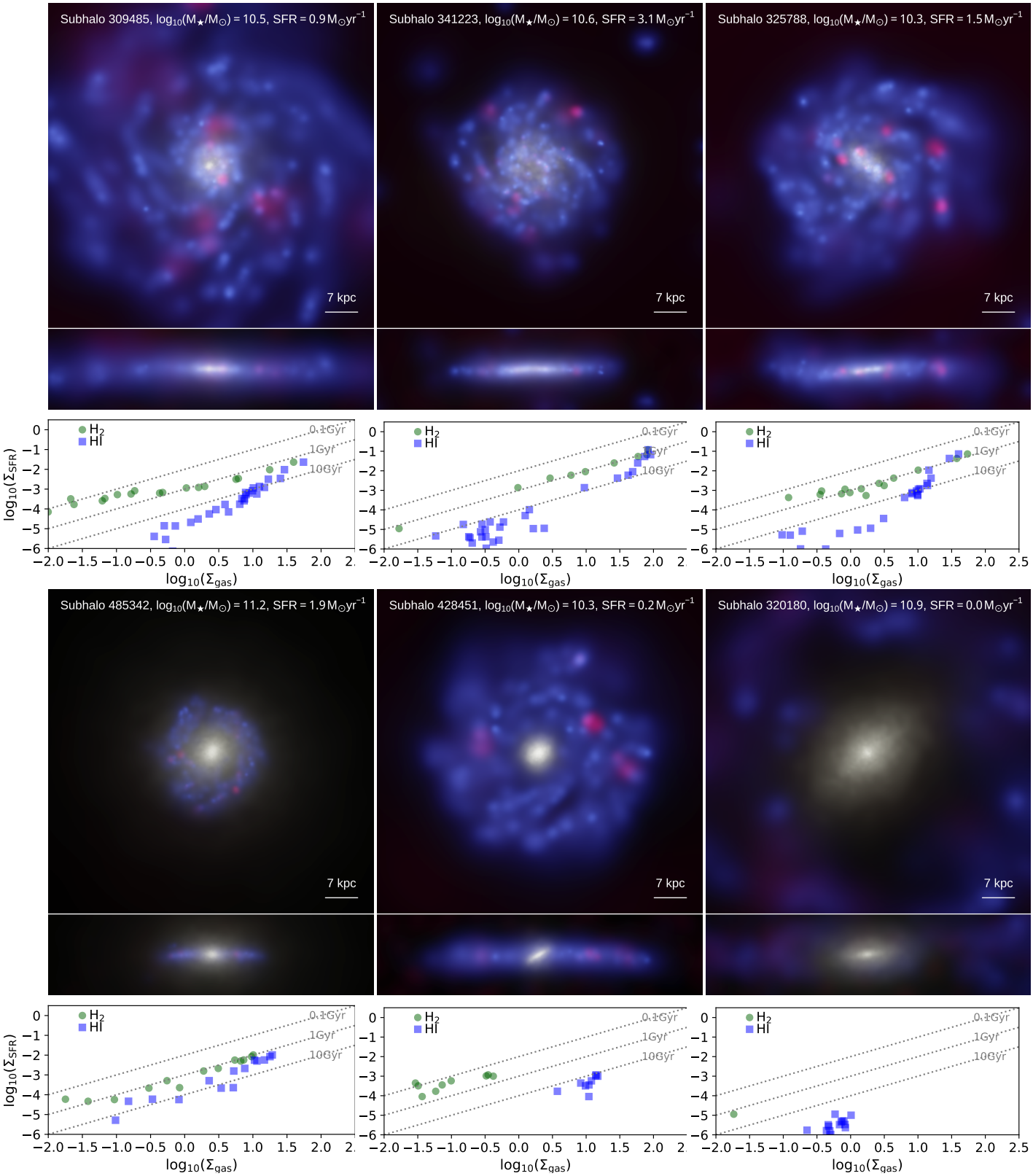

Figure B1. As Fig. 1 but for another 6 galaxies at $z = 0$ in the L025m6 run. The top row shows examples of star-forming galaxies, while the bottom row shows examples of galaxies below the main sequence but that still have some gas left to form stars.